TÉCNICO LISBOA

Model and Control of a Solar Tower for Energy Production

Kevin do Coito Ramos

Thesis to obtain the Master of Science Degree in

Aeronautical Military Sciences in the speciality of Electrical Engineering

Supervisors: Prof./Dr. João Manuel Lage de Miranda Lemos
Prof./Dr. Bertinho Manuel D'Andrade da Costa

Examination Committee

Chairperson: Prof./Dr. João Fernando Cardoso Silva Sequeira
Supervisor: Prof./Dr. João Manuel Lage de Miranda Lemos
Members of the Committee: BGEN/ENGEL Luis Filipe Basto Damásio
TCOR/ENGEL Ana Paula da Silva Jorge
Prof./Dr. Alexandre José Malheiro Bernardino

December 2015

The starting point of all achievement is desire.

Napoleon Hill

Acknowledgments

I would first like express my gratitude to the Portuguese Air Force Academy for the personal and school education administered and to Instituto Superior Técnico for the contribution to my graduation. Also, i manifest my profound appreciation to my mentor Professor João Miranda Lemos for the immense knowledge, advice and inspiring way that he guided me throughout the master thesis.

I would like to thank my family for the endless support, patient and care provided during my academic years. Also, to my friends for the joy, incentive and help.

A very special thanks to Andreia Santos for her incessant presence, belief and encouragement, supporting me spiritually.

Part of the work reported in this dissertation was performed within the framework of the project STAGE-STE (project number 609837) supported by the European Comission under the FP 7 programme.

Abstract

Solar towers are electrical power production systems that use highly concentrated solar radiation as energy source that is collected by means of a heat-transfer fluid. This master thesis studies the application of several control strategies with the aim of maintaining the working fluid at a temperature that maximizes the electrical production. The main difficulties are the nonlinear fluid temperature dynamics, plant thermal constrains, and a variable energy source that cannot be manipulated.

The temperature dynamics flow dependence demands for a changing parameter controller that results from a gain scheduling scheme or from a multi-model adaptive control strategy, in which the manipulated variable is adjusted by one of the set of local controllers designed for different operating regimes. The former is accomplished through a Proportional-Integral Controller (PI) control and the latter via Linear Quadratic Gaussian (LQG) optimal control. In addition, the Multistep Multivariable Adaptive Regulator (MUSMAR) control algorithm that adjusts its gains to every plant dynamic change, including parameters, is tested. Although the mentioned control concepts are applied considering the flow as the only manipulated variable, the combination of the latter with the radiation flux reflected by the heliostat field is also studied through PI control.

The solar tower electrical power production has a maximum for a given outlet temperature that changes with plant parameters and disturbances. The improvement of production levels is conducted by adjusting the temperature reference with a static optimization procedure.

Keywords

Solar tower model, PI control, LQG control, MUSMAR, coordination, static optimization

Resumo

As torres solares são sistemas de produção de energia elétrica que utilizam a radiação solar concentrada como fonte primária. A última, é absorvida por um fluído que percorre o permutador de calor em que a radiação incide. A presente dissertação estuda a aplicação de várias estratégias de controlo com o objetivo de manter a temperatura do fluido no valor que maximiza a produção de energia. As dificuldades principais centram-se na não linearidade da dinâmica da temperatura do fluído, nos limites térmicos do sistema e na incapacidade de manipular a radiação solar.

A alteração da dinâmica da temperatura com o caudal requer a utilização de um controlador de parâmetros variáveis que resulta de um esquema de escalonamento de ganhos ou da associação de diversos controladores projetados para diferentes pontos de operação. O primeiro método é desenvolvido com controlo PI enquanto que o último recorre ao controlo LQG. Em adição, é estudada a aplicação do algoritmo de controlo MUSMAR, em que os ganhos são adaptados para qualquer alteração da dinâmica do sistema, incluindo a variação de parâmetros do modelo. Embora as estratégias de controlo referidas considerem apenas o caudal como variável manipulável, a combinação da última com o fluxo de radiação é tambem estudada com um controlador PI.

A produção de energia de uma torre solar possui um máximo para uma dada temperatura que se altera com os parâmetros da planta e perturbações. O aumento da produção é conseguida pela determinação da referência de temperatura através de um algoritmo de otimização estática.

Palavras Chave

Modelo torre solar, controlo PI, controlo LQG, MUSMAR, coordenação, otimização estática

Contents

List of Figures

List of Tables

Abbreviations

ARMAX Auto Regressive Moving Average eXogenous

CRS Central Receiver System

CSP Concentrating Solar Power

DCSF Distributed Collector Solar Field

DNI Direct Normal Insolation

EPGS Electrical Power Generating System

GS Gain-Scheduling

LQE Linear Quadratic Estimator

LQG Linear Quadratic Gaussian

LQR Linear Quadratic Regulator

LTR Loop Transfer Recovery

MM Martin Marietta

MPC Model Predictive Control

NRMSE Normalized Root Mean Square Error

MUSMAR Multistep Multivariable Adaptive Regulator

PI Proportional-Integral Controller

PDE Partial Differential Equation

PRBS Pseudo Random Binary Sequence

PV Photovoltaic

RLS Recursive Least Squares

1

Introduction

Contents

Conventional power production systems use fossil fuels as a primary energy source. However, they are limited because they rely on a non-renewable resource and they cause a significant climate impact. The hydrocarbon availability reduction increases the oil price, allowing previously uneconomical energy sources to become economical to exploit. The renewable energy power generation systems are a possible alternative since they are environmental friendly and their fuel is derived from natural and unlimited resources.

The solar power reaching the earth surface is approximately 86,000 TW, which is far superior to the 15 TW global power consumption [5]. Thus, such energy source could represent a viable alternative to fossil fuels.

1.1 Motivation

Solar radiation energy can be directly converted to electricity using Photovoltaic (PV), or indirectly through Concentrating Solar Power (CSP). Although PV electricity production is popular, electricity production using CSP (the so called "solar thermal electricity",STE) has the current advantage of providing a mean for energy storage. Indeed, there are current industrial STE plants that are able to produce electrical power 24 hours per day. The last mentioned technology uses sun tracking mirrors (heliostats) to focus the sunlight onto a exchanger that absorbs energy through a heat transfer fluid, as water or molten salt. The collected energy can be stored in a thermal storage system that retains heat efficiently over days before being used in conventional electricity generation cycle as the Rankine or Brayton cycles [6]. Such systems range from a few kilowatts up to grid-connected power plants of hundreds of megawatts [7].

In contrast to conventional plants, solar power generating systems are unable to manipulate the energy source, that is variable. Therefore, CSP technologies must have a control scheme that handles solar radiation variation in order to regulate the fluid temperature and avoid plant thermal constraints infringement.

There are four main types of CSP systems: parabolic troughs, fresnel mirrors, dish engine, and solar towers or Central Receiver System (CRS). The last mentioned power generating system has a superior thermal efficiency compared to other CSP technologies due to a higher incident radiation flux concentration allowance that leads to superior working temperatures, and therefore to a higher efficiency. The heat exchanger represents the core of a CRS since it is where the major perturbation take place. In order to fully exploit such power generating systems capabilities, the results from applying different automatic control strategies must be studied.

1.2 State of The Art

The model for the outlet temperature of solar plants with distributed solar collectors has been developed via physical principles or empirically through data recovered from plant operation [8]. The solar tower dynamics is similar to the aforementioned plants and thus the receiver outlet temperature can also be described by a distributed parameter model given by a partial differential equation.

Several automatic control systems for the solar plants have been established. In [9], the quadratic-optimal control based on the linearized process dynamics of the steam boiler in a solar-powered central receiver is investigated and equations for the optimal regulator are given.

Under the distributed parameter model it was designed a nonlinear feedback linearization controller that showed improved results at plant startup [10]. In [11], a viable controller for tackling the collector optical efficiency uncertainty in ACUREX is addressed by combining the last mentioned technique with the Lyapunov based adaptation. The optimal control is derived for the last mentioned model in order to control the collector fluid velocity by maximizing the net energy collected, while also considering a bilinear lumped parameter model for the storage fluid temperature, the [12]. Furthermore, a static PI controller is explored in [11]. However, the change of the operating temperature and parameters uncertainties degrades the controlled system response. In the same work, successful results from applying the MUSMAR predictive adaptive controller are shown. The development of a variable sampling adaptive controller has proven to yield an increased control performance [13]. Experimental results demonstrated the capability of making fast temperature set-point changes with a reduced overshoot.

The existence of anti-resonance modes at process [14] motivated the development of an adaptive controller based on frequency methods to counter such dynamics [14]. The same approach was used to develop an internal model controller in [15].

Other approaches include the use of a neural network model within model based predictive control [16], and the application of predictive sliding mode controllers that have proved satisfactory results for reference tracking and disturbance rejection [17]. In addition, the flexibility at characterizing goals and constraints of the plant is achieved through fuzzy model based predictive control [18].

Regarding to optimal operation, the design and implementation of a two-layer hierarchical control strategy for a distributed solar collector field is described in [19]. The upper layer of the hierarchical strategy determines the optimal plant operating point while considering plant constraints and maximizing the profit from selling the electricity generated. However, the temperature dependence of the EPGS efficiency is set to be constant. In addition, a three layer algorithm is developed in [20], where the first layer computes the electrical power to be produced and delivered. The second layer computes the optimal set-point for the solar plant taking into account the information yielded from the first and economic profit optimization. The aforementioned work describes the DCSF through a concentrated parameter model. The simulation results presented demonstrate the benefit from using such hierarchic structure.

1.3 Objectives

The objective of this work is to develop and compare different control systems that maintain the outlet temperature of a CRS at a desired set-point, in the presence of disturbances. The controller must minimize the controlled variable deviation and guarantee that plant constrains are not violated, ensuring a lifetime of 20 to 30-years. The maximization of the solar tower electrical power production

by selecting the proper outlet temperature reference is also a goal.

1.4 Original Contributions

The main contributions of this master thesis are:

- Design of a solar LQG based tower receiver outlet temperature controller to improve power production.
- Development of a multi-model adaptive LQG controller for the outlet temperature of a CRS model.
- Testing of the MUSMAR control algorithm on the outlet temperature of a CRS model.
- Coordination between the fluid flow and the solar radiation flux as manipulated variables.
- Static optimization of a solar tower electric power production integrated with control strategies.

1.5 Thesis Outline

This master thesis is structured as follows: after the introduction, chapter 2 provides the problem description in which the plant to be controlled is detailed.

Chapter 3 addresses two modelling strategies, one arising from physical principles that result in a nonlinear model, and the other through data recovered from plant experiments, yielding a linear model that is only valid near a given operating condition.

Chapter 4 develops a PI, LQG and a predictive adaptive controller for the previously introduced process. Moreover, the coordination between two manipulated variables, the fluid flow and the solar radiation flux reflected by the heliostat field, is presented.

Chapter 5 focus on a hierarchic control structure that determines the optimal outlet temperature set-point that maximizes the plant electrical power production, considering process equilibrium functioning. Furthermore, an elasticity analysis to plant parameters and the influence of their estimation error at power production is assessed.

Chapter 6 provides comparative results obtained from the application of different control strategies for different simulation experiments.

Chapter 7 draws the conclusions and future developments to be done on the subject.

2

Problem Description

Contents

The maximization of the electrical energy production while maintaining plant integrity is achieved by overcoming several difficulties. The main operating challenge regarding solar towers is the flux concentration variation over the heat-exchanger due to changing environmental conditions, such as solar radiation availability, cloud transients, atmospheric moisture, solar position, and plant configuration. The aforementioned disturbance may cause irreversible damages to the receiver by violating plant thermal constraints and causing a negative effect on the CRS efficiency. In order to prevent such consequences, it is mandatory to develop an automatic control system. However, the control problem at hand is harsh due to plant uncertainties and considering that the main disturbance time constant is small when compared to the overall process. Moreover, the heat exchanger has nonlinear dynamics since the fluid specific heat and density are temperature dependent, and the system response rate varies with flow and temperature. Such plant characteristics demand for a varying parameter controller *i.e*, whose para meters depend on the operating regime.

The receiver fluid outlet temperature is maintained at the desired value by manipulating the fluid flow or via coordination between the former variable and the solar radiation power reflected by the heliostat field. The controlled variable that maximizes the solar tower efficiency depends on the plant disturbances, parameter variation and thermal losses. The solar tower used as a model for controller development purpose is the Solar Two power plant that is described in the following sections. In this chapter, the receiver system and the heliostat field are is addressed.

2.1 Solar Tower Description

Solar power towers use hundred of heliostats to focus the sun energy on a heat-exchanger located on the top of a tall tower, as shown in figure 2.1. The concentrated solar radiation is captured and stored at a hot tank, in thermal form, by means of a heat transfer fluid that flows through the tower receiver. The stored energy can be extracted to a steam generator that is connected to a conventional turbo-generator in order to produce electrical power. The resulting cooled fluid obtain from passing the molten salt through the steam generator is driven to the cold storage tank, where it is pumped to the heat-exchanger by means of flow controlled vale. The nominal inlet and outlet temperatures are $T = 290^oC$ and $T = 565^oC$, respectively. The valve flow is controlled in order to maintain a constant outlet temperature since solar radiation varies.

Although figure 2.1 only illustrates one receiver flow path and one valve, the solar tower considered as a paradigm in this thesis has a doubled fluid circuit, with two valves, for the east and west parts of the receiver.

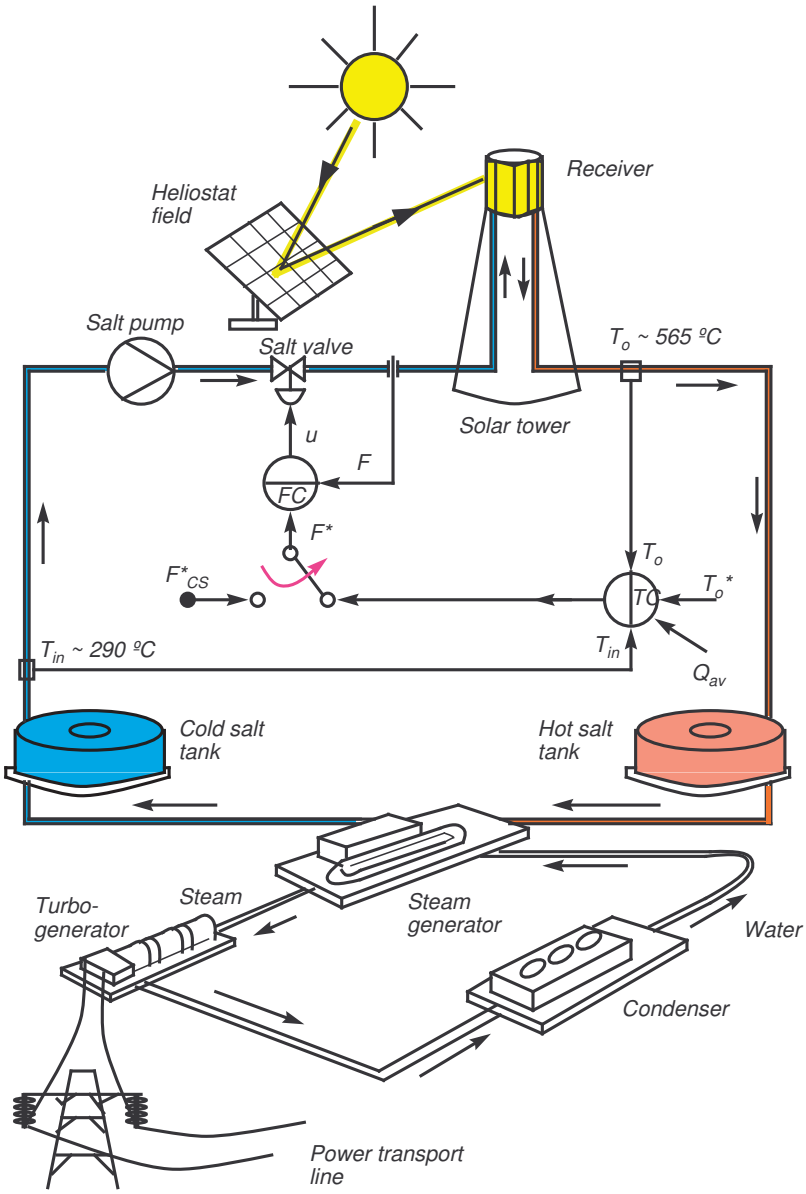

Figure 2.1: The main circuits in a solar tower power plant.

2.2 Solar Two Receiver System

In this thesis the Solar Two plant is taken as a paradigmatic example. Its receiver system was rated to absorb 42.2 MW of thermal energy at an average flux of 430 kW/m^2, while accommodating peak fluxes up to 800 kW/m^2 [21]. The flux distribution design allowed the salt temperature to increase from 290°C to 565 °C.

The heat exchanger consisted of an arrangement of 24 panels assembled in a cylindrical exposed configuration, as illustrated in figure 2.2. Every panel had 32 thin-walled, stainless steel tubes connected at both ends, where the heat transfer fluid circulated [6]. The external surfaces of the tubes were coated with paint that was resistant to high temperatures and thermal cycling, and absorbed 95% of the incident light [21]. Table 2.1 [1] details the technical characteristics of the receiver system.

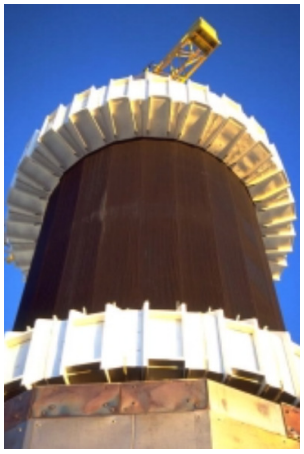

Figure 2.2: Solar Two receiver [1].

The heat transfer fluid circuit was divided in two paths that began from north and ended at south, as shown in figure 2.3. One had their own flow control valve and four photometers that sensed the incident radiation power. The outlet temperature T depends on the energy output of both paths accordingly to,

$$\dot{m}_{1+2}\rho_f cT- = \dot{m}_1\rho_f c_f T_1 + \dot{m}_2\rho c_f T_2 \Leftrightarrow T = \frac{\dot{m}_1}{\dot{m}_1 + m_2}T_1 + \frac{\dot{m}_2}{\dot{m}_1 + m_2}T_2, \tag{2.1}$$

where $T_{1,2}$ and T_{in} are the outlet and inlet temperature of each receiver circuit , $\dot{m_{1,2}}$ is the mass flow rate, ρ_f is the fluid density and c_f is the fluid specific heat.

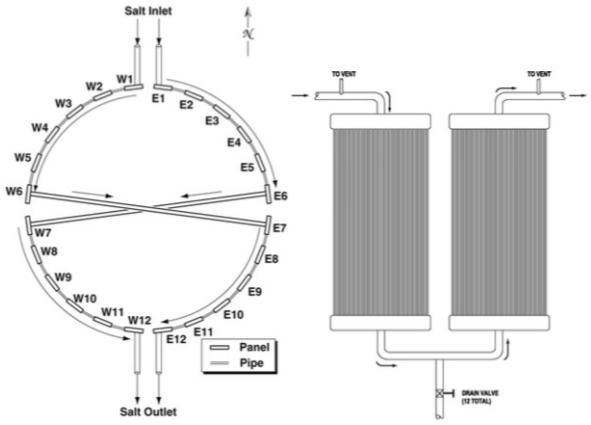

Figure 2.3: The Solar Two flow pattern, viewed from top (LEFT) and flow arrangement between two adjacent receiver panels (RIGHT) [2]

.

Table 2.1: Technical characteristics of the Solar Two Receiver [1].

Description	Value
Inlet Temperature	290 °C
Outlet Temperature	565 °C
Ambient Temperature	21 °C
Peak Radiation Flux	800 kW/m^2
Average Radiation Flux	430 kW/m^2
Panels	24
Flow Circuits	2 (12 panels each)
Tubes/panel	32
Tubes Outward Diameter	2.1 cm
Wall Thickness	1.2 mm
Absorber Height	6.2 m
Absorber Diameter	5.1 m
Absorber Area	99.3 m^2

2.2.1 Valve

The receiver outlet temperature is maintained at a desired value by manipulating the molten salt flow rate. For this purpose, the heat exchanger is equipped with one flow controlled valve per circuit, wherein the flow reference is modulated through a temperature control algorithm. Since the fluid paths are designed to minimize the collected energy difference between circuits, only one control signal for both valves is developed. Thus, less computation effort is required. The valves are represented by a first order system where $T_v = 5s$ is the time constant. The actuator mathematical model in the frequency domain is written as,

$$\frac{Y(s)}{U(s)} = \frac{1}{T_v s + 1}, \tag{2.2}$$

where $Y(s)$ and $U(s)$ are the valve output flow and reference, respectively.

The applied control strategy is a Proportional-Integral Controller (PI) in a simple fault tolerant configuration, as shown in figure 2.4. Therefore, the failure of one valve leads to a flow increase at the other, reducing potential problems related to excessive temperature or pressure. The controller parameters are design to achieve a step response rise time of $T_r \approx 11s$.

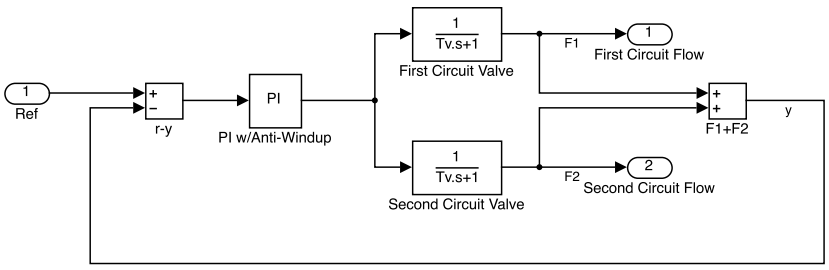

Figure 2.4: PI valve controller applied in a fault tolerant structure.

2.2.2 Heat Transfer Fluid

The use of molten salt mixture as a heat transfer fluid is advantageous since the oil has high volumetric heat capacity, low conductivity, compatible operating temperatures with high-pressure and high-temperature steam turbines and is a low-cost medium in which to store thermal energy. The Solar Two used nitrate salt composed by 60% of sodium nitrate ($NaNO_3$) and 40% of potassium nitrate (KNO_3). The melted salt operating temperatures range from 260°C to approximately 621°C. It solidifies at 221°C and crystallises at 238°C [22]. In liquid state, the variation of the fluid proprieties as a function of temperature T, between 300 to 600°C, are given by the following expressions [22],

$$\rho_f(T) = 2090 - 0.636 \times T, \qquad [\text{kg m}^{-3}] \quad (2.3)$$

$$c_f(T) = 1143 + 0.172 \times T, \qquad [\text{J kg}^{-1}\,^{\circ}\text{C}^{-1}] \quad (2.4)$$

$$k_f(T) = 0.443 + 1.9 \times 10^{-4} \times T, \qquad [\text{W m}^{-1}\,^{\circ}\text{C}^{-1}] \quad (2.5)$$

$$\mu_f(T) = \frac{22.714 - 0.12T + 2.281 \times 10^{-4}T^2 - 1.474 \times 10^{-7}T^3}{1000}, \qquad [\text{Pa s}^{-1}] \quad (2.6)$$

where ρ_f, c_f, k_f and μ_f are the density, specific heat, thermal conductivity and dynamic viscosity, respectively.

2.3 Solar Two Heliostat Field

The Solar Two heliostat field consisted of 1818 Martin Marietta (MM) solar reflectors of 39.1 m^2 each and 108 Lugo heliostats of 95 m^2 each, which resulted in a total reflector area of 81400 m^2 [1]. The mirrors had an average clean reflectivity of 0.903 and 0.94, respectively, and were installed at a distance between 105 and 235 m [1]. Table 2.2 details the technical characteristics of the mirrors.

Table 2.2: Technical characteristics of the Solar Two heliostats [1].

MM Heliostats	
Number	1818
Reflective area	39.13 m^2
Number of Mirror Modules	12
Clean Reflectivity	0.903
Total MM Heliostat Field Area	71140 m^2

MM Heliostats	
Number	108
Reflective area	95 m^2
Number of Mirror Modules	16
Clean Reflectivity	0.94
Total Lugo Heliostat Field Area	10260 m^2

3

Process Modeling

Contents

In control theory, a model is a mathematical representation of a system that allows the study of its dynamics through analysis and simulation and, upon convenient simplifications, forms the basics for design [23]. This work presents two models of the Solar Two CRS, one developed via physical principles and the other by input/output data collected from tests performed at the plant. The first method yields a nonlinear continuous model that allows the inspection of the system behaviour as a consequence of modifying parameters or variables, whereas the latter results in a linear discrete model that is only valid near a given operating point but that has the advantage of allowing controller design. Since Solar Two no longer exists, the data is gathered using simulations in the first model.

3.1 Reduced Complexity Model

The dynamics of a solar tower receiver is modelled by an hyperbolic partial differential equation, obtained from energy conservation. The fluid temperature is described by a scalar function $T(z,t)$ where $z \in \Re$ is a space dimension measured along the pipe, and $t \in \Re$ is continuous time [3]. The corresponding equation is derived from the analysis of the net enthalpy in time and space, in a small section of pipe between z and $z + \Delta z$, as shown in figure 3.1. The system thermodynamic potential variation between time instants t and $t + \Delta t$, considering an incompressible fluid and no diffusion, is given by [3],

$$E_1 = \rho_f c_f A_f \Delta z \big[T(z, t + \Delta t) - T(z, t)\big],$$

where T is the temperature, ρ_f is the fluid density, c_f is the specific heat, and A_f is the pipe's cross section area.

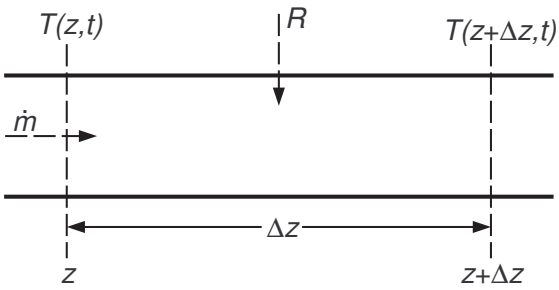

Figure 3.1: An element of the pipe in a receiver system and the variables used to develop the PDE model [3].

The net enthalpy in space between t and $t + \Delta t$, is given by the sum of two terms. The first, is the enthalpy difference entering and leaving the pipe element due to fluid flow $\dot{m}(t)$,

$$E_2 = \rho_f c_f \dot{m}(t) \Delta t \big[T(z,t) - T(z + \Delta z, t)\big].$$

The second, is the enthalpy increase due to solar energy,

$$E_3 = \bar{\alpha} R(t) \Delta z \Delta t,$$

where R is the solar radiation power and $\bar{\alpha}$ is a parameter related to the efficiency of the energy absorption by the fluid that depends on fluid thermal characteristics and also on mirror optical efficiency and geometry [3]. Therefore,

$$E_1 = E_2 + E_3,$$

or,

$$\rho_f c_f A_f \Delta z \big[T(z, t+\Delta t) - T(z,t)\big] = \rho_f c_f \dot{m}(t) \Delta t \big[T(z,t) - T(z+\Delta z, t)\big] + \bar{\alpha} R(t) \Delta z \Delta t. \tag{3.1}$$

Rearranging (3.1), the fluid velocity emerges,

$$F = \frac{\dot{m}}{A_f},$$

and α is defined as,

$$\alpha \triangleq \frac{\bar{\alpha}}{\rho_f c_f A_f}.$$

The partial differential equation is obtained by approaching time and space intervals to infinitesimal values, yielding

$$\frac{\partial}{\partial t} T(z,t) = -F \frac{\partial}{\partial z} T(z,t) + \alpha R(t). \tag{3.2}$$

In order to consider thermal losses to the environment, the loss coefficient term γ is added to the model,

$$\frac{\partial}{\partial t} T(z,t) = -F \frac{\partial}{\partial z} T(z,t) + \alpha R(t) - \gamma (T_{av}(z,t) - Ta). \tag{3.3}$$

where T_{av} and T_a are the average and ambient temperature, respectively. The resulting nonlinear equation describes the dominant dynamics of a solar tower receiver with one fluid circuit.

3.1.1 Finite dimension state space

The infinite dimension model given by equation (3.3) is approximated by projecting the spacial dependence on a finite dimensional set. The states are the temperature of points equidistantly located at $z = 0$, $z = \Delta z$,..., $z = n\Delta z$, where n is the number of points in the grid, as shown in figure 3.2. In this work, n is equal to the amount of panels over the fluid's path. Each state $x_i(t)$ is defined as the fluid temperature at position $i\Delta z$,

$$x_i(t) \triangleq T(i\Delta z, t).$$

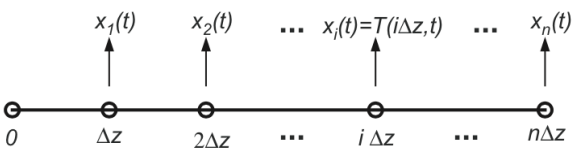

Figure 3.2: Space grid representation of the finite dimension state-space model [3].

The PDE model can be approximated with respect to z, using backward finite differences,

$$\frac{\partial}{\partial t} T(z,t) \approx \frac{T(z,t) - T(z-\Delta z, t)}{\Delta z}.$$

The resulting description of the PDE model is given by a set of ordinary differential equations for $i = 1, ..., n$,

$$\frac{dx_i}{dt} = -F(t)\frac{1}{\Delta z}(x_i(t) - x_{i-1}(t)) + \alpha R(t) - \gamma\Big(\frac{(x_i(t) + x_{i-1}(t)}{2} - T_a\Big). \tag{3.4}$$

The convenient temperature measure for feedback purposes is registered at the pipe outlet. Since the receiver to be modelled has two flow circuits and considering equation (2.1), the output equation is given by,

$$y(t) = \frac{F_P^1}{F_P^1 + F_P^2}x_n^1 + \frac{F_P^2}{F_P^1 + F_P^2}x_n^2, \tag{3.5}$$

where $x_n^{1,2}$ and $F_P^{1,2}$ is the outlet temperature and fluid velocity of each path, respectively. The latter is found by multiplying F by the number of tubes of the receiver panel. Defining the state vectors for each circuit $x^{1,2}$ as the temperature per panel,

$$x^{1,2} = \big[x_1^{1,2} \dots x_n^{1,2}\big],$$

and the parameter matrices,

$$\Xi = \big[1 \dots 1\big]^T,$$

$$\vec{e}_1 = \big[10 \dots 0\big]^T,$$

and,

$$B = -\frac{1}{\Delta z}\begin{bmatrix} 1 + \frac{\gamma}{2}\Delta z & 0 & \dots & 0 \\ -1 + \frac{\gamma}{2}\Delta z & 1 + \frac{\gamma}{2}\Delta z & \ddots & \vdots \\ \vdots & \ddots & \ddots & 0 \\ 0 & \dots & -1 + \frac{\gamma}{2}\Delta z & 1 + \frac{\gamma}{2}\Delta z \end{bmatrix}.$$

The state-space model for each receiver circuit can be written in compact form as,

$$\begin{cases} \dot{x}^1 = x^1 B F^1 + \alpha \Xi R + \vec{e}_1\Big(\frac{F^1}{\Delta z}T(0,t) + \gamma T_a\Big). \\ \dot{x^2} = x^2 B F^2 + \alpha \Xi R + \vec{e}_1\Big(\frac{F^2}{\Delta z}T(0,t) + \gamma T_a\Big). \end{cases} \tag{3.6}$$

The parameters and coefficient values used to model the Solar Two receiver are specified in table 3.1. The value of $\bar{\alpha}$ is determined through simulation considering a total nominal flow of $F = 80\ kg/s$ and rated radiation flux. Furthermore, the loss coefficient is specified so that the system dissipates an average power loss of $1.6MW$, at nominal operation. The pipe element length is considered to be the flow path width divided by the number of panels.

Table 3.1: Parameters and coefficients used to model the Solar Two receiver system.

Description	Symbol	Value
Absorption and mirror efficiency	$\bar{\alpha}$	$6.70 \times 10^{-3}\ m$
Loss coefficient	γ	$8.56 \times 10^{-4}\ s^{-1}$
Pipe element length	Δz	7.96 m
Nominal flow Rate	F_T	80 kg/s
Circuit maximum flow Rate	F_T^{max}	110 kg/s

3.1.2 Plant Dynamics

In order to enhance the understanding of the solar tower receiver model given by equation (3.3), several *MATLAB* simulations are presented. Neither the extra delay of the solar radiation action due to green-house effect nor the valve dynamics are considered.

The first analysis on the receiver dynamics is conducted by the examination of the the system response in the absence of losses and solar radiation. Moreover, it is assumed that the temperature of the fluid entering the pipe is time constant and equal to $T(0,t) = 0$. Such considerations reduces equation (3.3) to the advection equation given by,

$$\frac{\partial}{\partial t}T(z,t) = -F\frac{\partial}{\partial z}T(z,t). \tag{3.7}$$

The transport of the temperature at the foremost panel of the receiver, along the flow path, considering constant and nominal input F, is shown in figure 3.3.

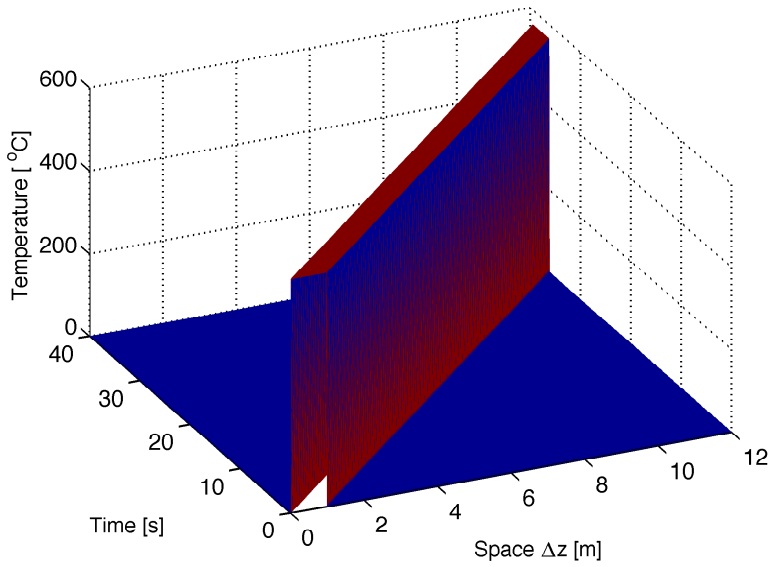

Figure 3.3: Temperature transport through one receiver flow circuit.

The *loci* over the plane $[z,t]$, for which $T(z,t)$ is constant in time are denominated characteristic lines and are given by the solution of the differential equation,

$$\frac{dz}{dt} = F. \tag{3.8}$$

Figures 3.4 and 3.5 illustrate examples of the solution of equation (3.8), for constant fluid flow. The increase of the input variable F decreases the time necessary for the output temperature to be affected.

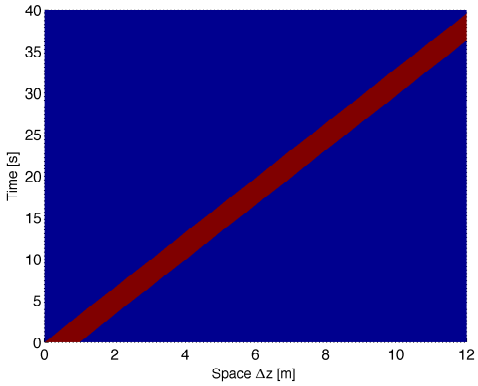

Figure 3.4: Characteristic lines for nominal flow.

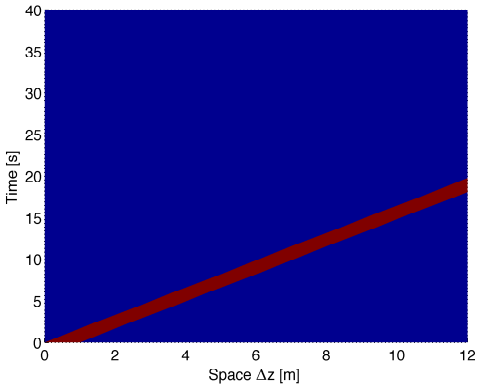

Figure 3.5: Characteristic lines for a flow twice higher than nominal.

Hereafter, the analysis on the system dynamics considers the existence of solar radiation, temperature losses and fluid entering the pipe with $T(0,t) = 290^oC$. The former perturbation leads to a temperature rise along the receiver's flow path, ascending from the inlet to the outlet. The output temperature can be adjusted by varying the fluid exposure time to solar radiation that changes the amount of energy absorbed. Figure 3.6 shows the model response to a step on the fluid flow, with constant and equal radiation through the receiver. It can be concluded that the system has an inverse response. The temperature increases as the flow decreases.

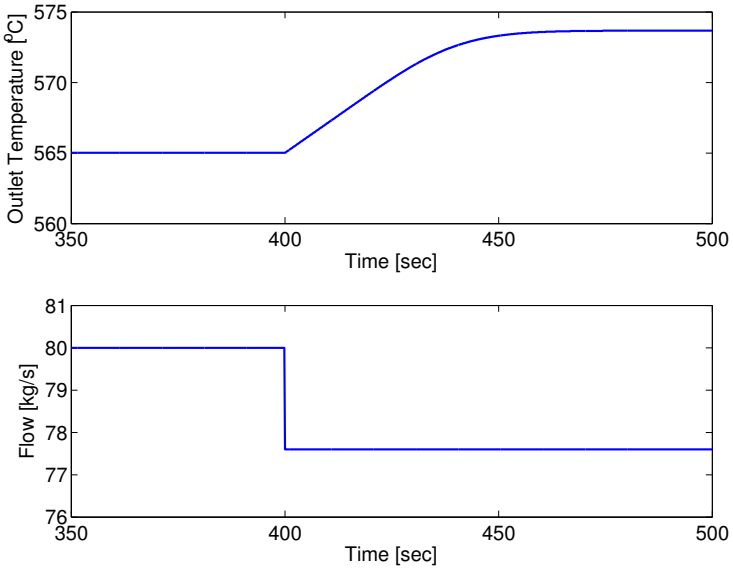

Figure 3.6: Outlet temperature response to a input step decrease of 3% from the nominal value.

In steady state, the temperature distribution along the pipe is approximately represented by a straight line. The increase of thermal losses reduces temperature and increases the bending of the aforementioned line. The transient between equilibrium points in the $[T, Z]$ plane is illustrated in figure 3.7.

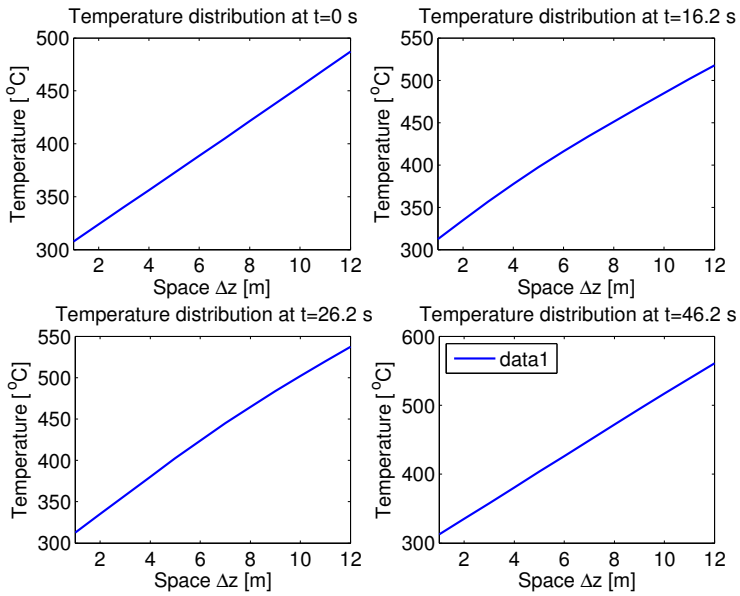

Figure 3.7: Temperature distribution between equilibrium points.

The model response to a step on the fluid flow in a three dimensional axes is represented in figure 3.8.

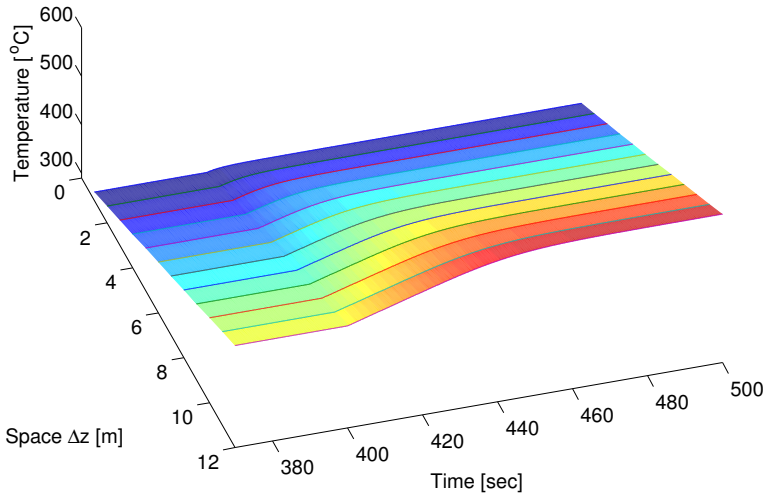

Figure 3.8: Outlet temperature response to an input step from $F_T = 104.7\ kg/s$ to $F_T = 72\ kg/s$.

The application of an input step variation with equal magnitude for different operating points is illustrated in figure 3.9. The effect of reducing the flow increases the output amplitude, rise time and settling time, as the working temperature rises. The system response to distinct incident solar radiation power and thermal losses coefficient is shown in figures 3.10 and 3.11, respectively. The variation of these variables only modifies the output response amplitude.

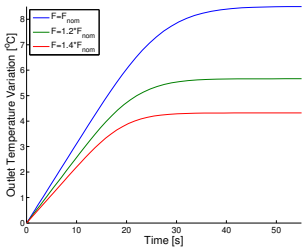

Figure 3.9: Outlet temperature variation due to an input step decrease of 3% of nominal value, for different operating points.

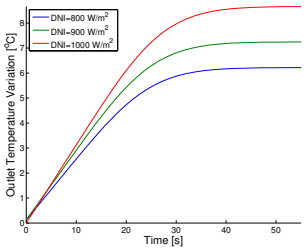

Figure 3.10: Outlet temperature variation due to an input step decrease of 3% of nominal value, for different incident radiation power.

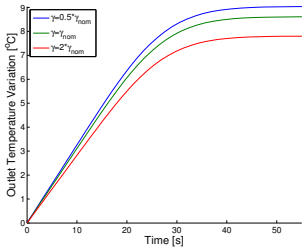

Figure 3.11: Outlet temperature variation due to an input step decrease of 3% of nominal value, for different loss coefficient.

Hitherto, constant values for model parameters and disturbances have been considered, although most alter with time. The major perturbation is the radiation flux concentration that may change due to atmospheric moisture or passing clouds that cause fast changes of low or high amplitudes. Moreover, the Direct Normal Insolation (DNI) varies due to the apparent movement of the sun. Figures 3.12 and 3.13 illustrate these disturbances effect on the outlet temperature, with constant and nominal flow. In the absence of a controller, solar energy is underused and the infrastructure is exposed to high thermal stress.

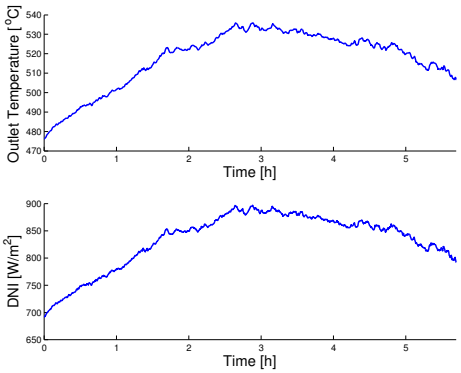

Figure 3.12: Outlet temperature variation due to atmospheric moisture and the apparent movement of the sun.

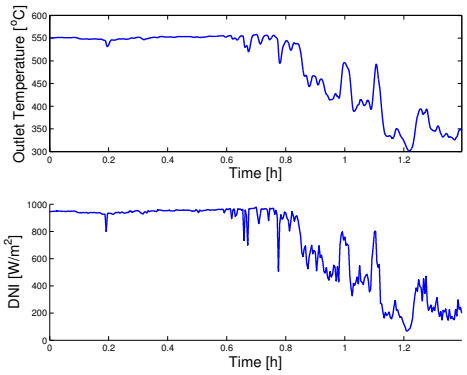

Figure 3.13: Outlet temperature variation due to passing clouds.

3.2 System Identification

System identification is the experimental method for process modeling and comprises: experimental planning; selection of model structure; criteria; parameter estimation and model validation [4]. The process modeling presented is discrete time-based and it is established through a polynomial approach. The system identification is conducted between the input flow u of the controlled valve and the outlet temperature y, while maintaining all the perturbations constant. Figure 3.14 illustrates the *MATLAB Simulink* block model of the process to be modelled.

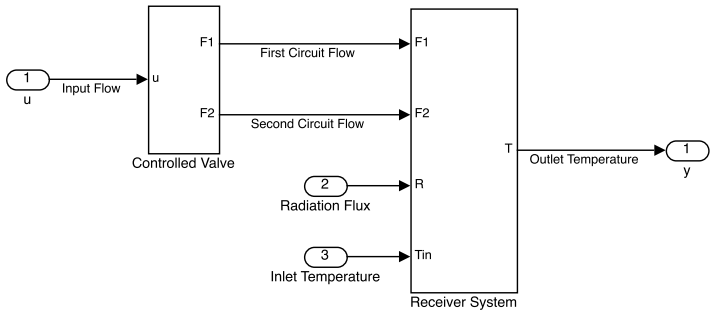

Figure 3.14: *MATLAB Simulink* model of the system used for identification purpose.

A good representation of the plant transient response, without allowing to the appearance of non-minimum-phase zeros or a too extensive open loop functioning between sampling instants, is achieved by choosing a sampling period ten times smaller than the rise time, T_r [4]. In order to avoid nonlinearities, T_r is determined by the step response of a reference amplitude reduction of 3% of the nominal flow $F_T = 80\ kg/s$. The resulting sampling period is $T_s \approx 4s$.

3.2.1 Experimental Planning

The experimental plan aims to establish the strategy to collect the most appropriate input-output information for model construction. The input signal must avoid the appearance of nonlinearities and excite every possible modes of the process so that the plant output clearly exhibits the systems dynamics, in the desired bandwidth. Since a computer model is used for identification purposes, a high duration signal may be applied without suffering from the influence of solar radiation drifts [8]. Thus, a Pseudo Random Binary Sequence (PRBS) with binary values of $\pm$ 3% from the operating point flow rate is applied, in order to avoid the appearance of nonlinearities.

The model can be built without modeling the absolute values, since it describes the responses for deviations from a physical equilibrium. Thus, the mean of the input and output signals are removed, as well as the initial transient.

3.2.2 Model Structure,Parameter Estimation and Criteria

The modeling approach presented assumes that the system is unknown and that all model parameters are adjusted without considering physical information. Thus, it is represented by a black-box model. The Auto Regressive Moving Average eXogenous (ARMAX) structure is adequate to use since the system noise is coloured and the process has load perturbations. Such model is given by the following expression,

$$A(q^{-1})y(h) = B(q^{-1})u(h - n_k) + C(q^{-1})e(h)$$

where $e(h) \in \mathbb{R}$ is a Gaussian white-noise disturbance, q^{-1} represents the backward shift operator, n_k is the value of the pure delay and,

$$A(q^{-1}) = 1 + a_1 q^{-1} + \ldots + a_{n_a} q^{-n_a}$$

$$B(q^{-1}) = 1 + b_1 q^{-1} + \ldots + b_{n_b} q^{-n_b}$$

$$C(q^{-1}) = 1 + c_1 q^{-1} + \ldots + c_{n_c} q^{-n_c}.$$

where n_a, n_b, n_c and n_k are the tuning variables. The polynomial coefficients are estimated through the quadratic prediction error criterion that avoids parameter estimation polarization, using *armax MATLAB* function.

3.2.3 Model Validation

The model validation aims to verify if the identified model reproduces the system behaviour within acceptable bounds. This is accomplished by comparing model and measured output, step responses and residual analysis. The presented results are developed for the nominal operating point.

The goodness of fit between the obtained model and the data collected from the plant test is measured through the Normalized Root Mean Square Error (NRMSE), that is given by

$$fit(\%) = 100 \times \left(1 - \frac{\sqrt{\sum_i (y_i - \hat{y}_i)^2}}{\sqrt{\sum_i (y_i - \bar{y}_i)^2}}\right).$$

where y_i and $bary_i$ are the nonlinear model response and respective mean value and $\hat{y}_i$ the linear model output for the sample i. The setting parameters that yields the best results of the above-mentioned function are: $n_a = 10$, $n_b = 3$, $n_c = 10$ and $n_k = 1$. The estimated coefficients are stated in appendix B. Figure 3.15 illustrate the comparison between outputs and the goodness of the fit. The identified model response accurately represents the measured output signal.

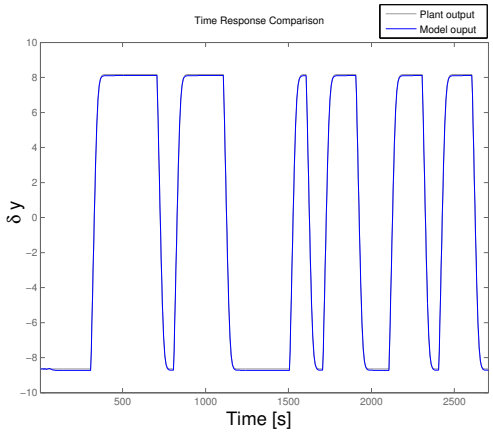

Figure 3.15: Comparison between model and measured output with a NRMSE of 98.83 %.

The outlet temperature variation of the nonlinear and linear model due to different input steps are illustrated in figures 3.16, 3.17 and 3.18. The dynamics of both models are similar however, the steady state error between outputs varies with the input step amplitude. Although, for an input change of 5%, the output deviation between models is $\delta T = 0.72^o C$, which is neglectable when comparing to the overall output temperature $T = 579.76^o C$. In addition, symmetric input step values cause a slightly different output temperature variance. This phenomenon is due to the variation of the fluid proprieties

with temperature. Figure 3.19 illustrate the system response to a input step decrease of 3% of the working fluid, when operating at an outlet temperature of $T = 535^oC$. The output error percentage is superior to the nominal operating condition.

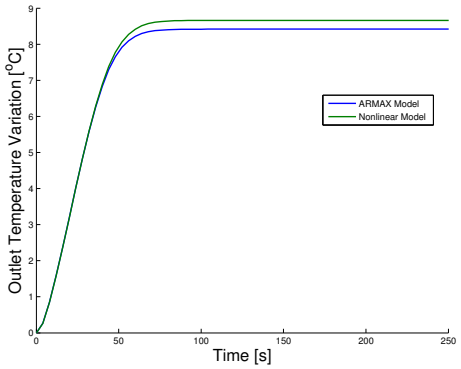

Figure 3.16: Nonlinear and linear model response to a input step decrease of 3% from nominal value.

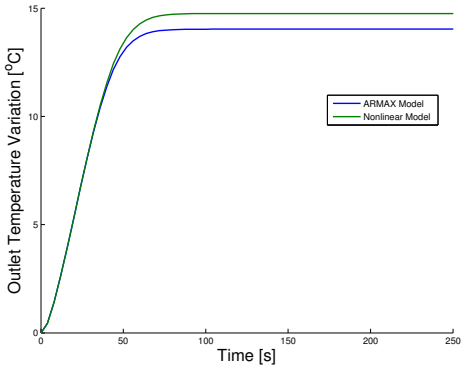

Figure 3.17: Nonlinear and linear model response to a input step decrease of 5% from nominal value.

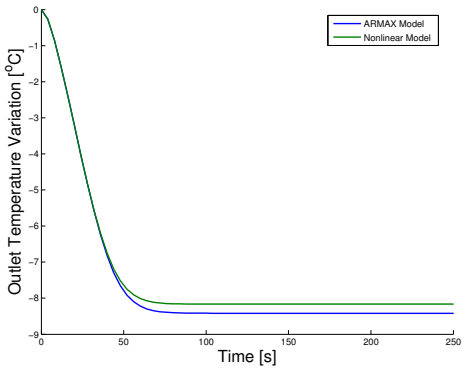

Figure 3.18: Nonlinear and linear model response to a input step increase of 3% from nominal value.

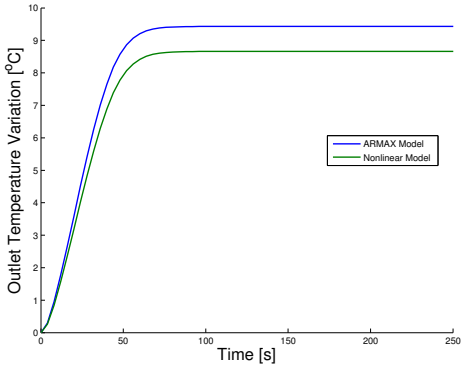

Figure 3.19: Nonlinear and linear model response to a input step decrease of 5% of operating point, for a working temperature of $T = 535^oC$.

The residual analysis comprises the whiteness and independence tests that verify if the outlet temperature residuals are uncorrelated and if the contribution of the lagged input to the output is properly described by the model, respectively. The inquiry of these features is conducted by examining whether the residual autocorrelation function and the cross-correlation function, between the past inputs and the residuals, are limited within a confidence interval. Figure 3.20 illustrate the above mentioned functions with a confidence interval of 99%. It can be concluded that the model has the necessary statistical characteristics.

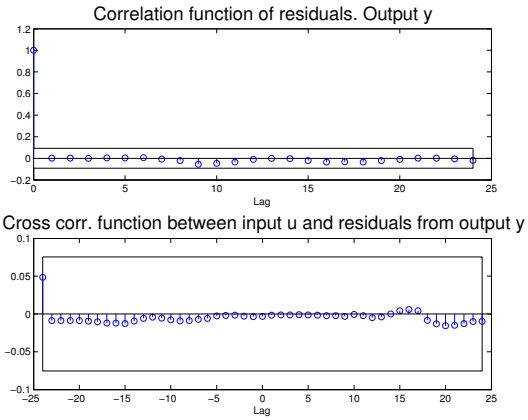

Figure 3.20: Output residual autocorrelation function (TOP) and cross-correlation function between the past input and the output residuals (BOTTOM), for a confidence interval of 99%.

4

Process Control

Contents

The system to be controlled comprehends a flow controlled valve in series with the receiver model in a cascade structure, as illustrated in figure 4.1. Such configuration is feasible since the valve has a dynamics faster than the fluid outlet temperature. The inner loop manipulates the flow, whereas the outer loop actuates over the outlet temperature by manipulating the flow reference.

The controller objective is to maintain the output variable at a specified reference, regardless of solar radiation variation. This intent is accomplished considering the existence of maximum and minimum flow and temperature constraints.

The control signal results from the combination of two independent terms. The first is derived from a feedback system that only reacts after the disturbance has taken effect at the receiver output. The second is a feed-forward contribution generated from the sensed DNI that compensates for disturbances before the outlet temperature is perturbed.

The nonlinear fluid temperature dynamics demand for a changing parameter controller that is achieved through a Gain-Scheduling (GS) scheme, a multi-model adaptive control structure, or a predictive adaptive controller.

In sections 4.1,4.2 and 4.4, the manipulated variable is the valve position, while in section 4.5 the solar radiation flux given by the heliostat field is also modulated.

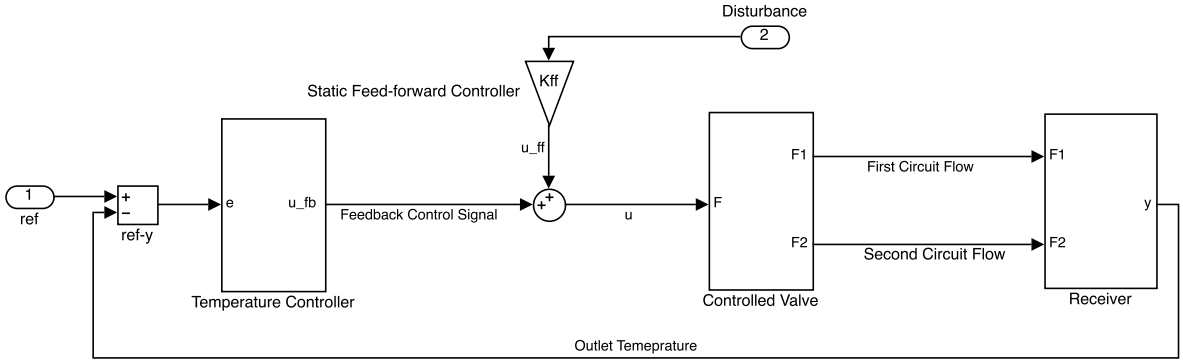

Figure 4.1: Plant outlet temperature controller scheme.

4.1 PI Control

The PI control concept uses the error between a measured process variable and the desired set-point to generate the manipulated variable, in a feedback loop. The control signal results from the sum of two contributions, one proportional to the error and the other proportional to the integral of the error. In continuous time yields,

$$u(t) = K_p\Big(e(t) + \frac{1}{T_i}\int_0^t e(\tau)d\tau\Big), \tag{4.1}$$

where u is the control variable and e the error. The controller tuning parameters are the gain K_p and integral time T_i [23]. The last mentioned values are designed using a modified Zielgler and Nichols ultimate sensitivity rule that does not require knowledge of the mathematical model of the system.

The existence of maximum and minimum valve position limits, require the existence of an anti-windup scheme to avoid continuous integral action above actuating boundaries. The latter aim is

accomplished by adding to the integrator the difference between the output of the model nonlinearity and the value given by the sum of the P and I actions, multiplied by a constant α. Thus, when the valve is saturated, the last mentioned term cancels the integration. Figure 4.2 illustrates the last mentioned controller block diagram.

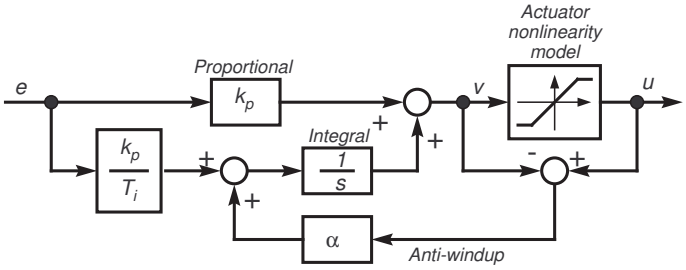

Figure 4.2: PI controller with anti-windup.

4.1.1 PI Controller Design

The PI controller parameters are designed using a modified Ziegler and Nichols ultimate sensitivity rule, since the standard formula yields a closed-loop response with excessive overshoot and oscillation. This method determines K_p and T_i as a function of the ultimate gain K_u and period T_u, as stated in table 4.1.

Table 4.1: Ultimate sensitivity rules [4].

	K_P	T_i
ZN ultimate sensitivity rule	$0.45K_u$	$0.833T_u$
Modified rule	$0.06K_u$	$0.17T_u$

The variables K_u and T_u are obtained with the process at stability limit, when a pure proportional controller with gain K_u is applied. This working condition corresponds to an oscillatory output with a constant yet unknown amplitude that may damage the plant. Such problem is overcome by using the relay feedback method that limits the oscillation amplitude. The scheme of the aforementioned procedure is illustrated in figure 4.3.

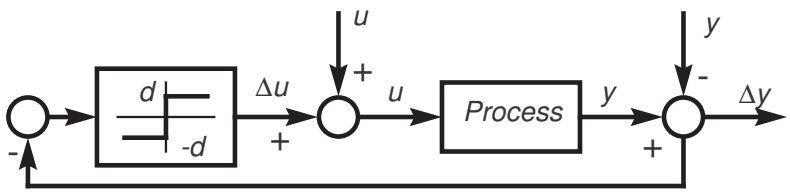

Figure 4.3: Block diagram of the relay feedback method applied to the process.

Figure 4.4 show the input and output signals obtained by applying the relay feedback method to the process for relay limit values of $d = \pm 0.08 F_{nom}$. It can be concluded that the plant attenuates higher frequencies and so, it is acceptable to consider the contribution of the first harmonic component of

the input signal only. These signals have opposite phase thus, the period of oscillation is the ultimate period T_u [24].

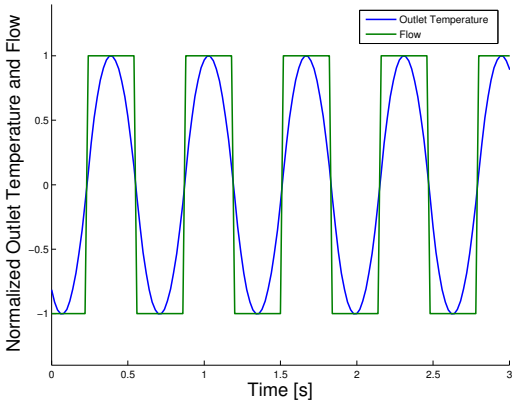

Figure 4.4: Input and output signals obtained by applying the relay feedback method to the process.

The plant gain at stability limit results from the ratio of the output amplitude a and the square wave first harmonic amplitude $4d/\pi$,

$$G(i\omega_u) = -\frac{\pi a}{4d}. \tag{4.2}$$

The describing function is a method to determine the condition for oscillation in a nonlinear feedback system composed by a linear element and a static nonlinearity. The former is the plant linear operation while working around the nominal point, whereas the latter corresponds to the relay. The nonlinear block is described by a gain $N(a)$ that represents how a sinusoid of amplitude a propagates through the system. The condition for oscillation of a process with transfer function $G(i\omega)$ is determined by requiring that the sine wave propagates with constant amplitude and phase,

$$N(a)G(i\omega) = -1. \tag{4.3}$$

The intersection of $-1/N(a)$ with the Nyquist curve $G(i\omega)$ indicates the possible occurrence of an oscillation. At the crossing point, the amplitude and frequency are equal for both plots. Therefore, the ultimate gain is equal to the relay describing function that is given by,

$$N(a) = \frac{4d}{\pi a}. \tag{4.4}$$

The use of a relay with hysteresis is advantageous since it avoids random switches caused by noise measurement. However, the hysteresis alters the cross point between $-1/N(a)$ and the Nyquist curve, leading to a gain and period different from the ultimate values. The describing function of a relay with hysteresis is,

$$N(a) = \frac{4d}{-\pi\sqrt{a^2 - \varepsilon^2} - i\pi\varepsilon}, \tag{4.5}$$

where ε is the hysteresis width that must be higher than the noise amplitude. Figure 4.5 illustrate the input and output signals obtained with the hysteresis relay feedback procedure for $d = \pm 0.08 F_{nom}$ and $\varepsilon = 15$. Hence, the process input only changes when a 15^oC error is verified. The resulting ultimate values are $T_u = 83s$ and $K_u = -2.53 \times 10^{-5}$. The input and output signal no longer have opposite phase, which confirms that the values of K_u and T_u do not characterize the stability limit.

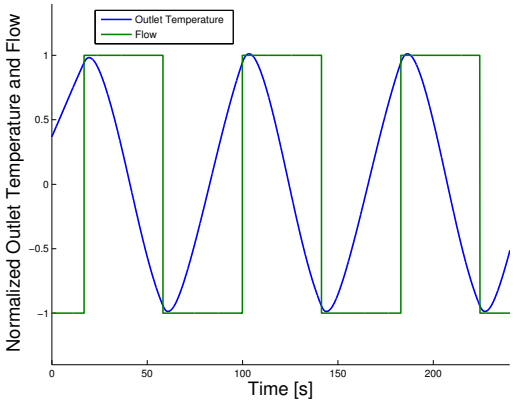

Figure 4.5: Input and output signals obtained by applying the relay with hysteresis feedback method.

The plant controlled and manipulated variables due to a reference step of 15^oC from nominal operating condition are shown in figure 4.6. The outlet temperature step response has a rise time of approximately 58 s and no overshoot. Figure 4.7 illustrate the same signals for different DNI. The outlet temperature rise time increases with the disturbance amplitude. Such behaviour is verified since the effect of the control effort reduces as the flow increases. The maximum temperature value of the presented experiment is $T_{max} = 580.7^oC$ for a DNI of 900 W/m^2. Thus, the step response overshoot is insignificantly changed for different DNI amplitude.

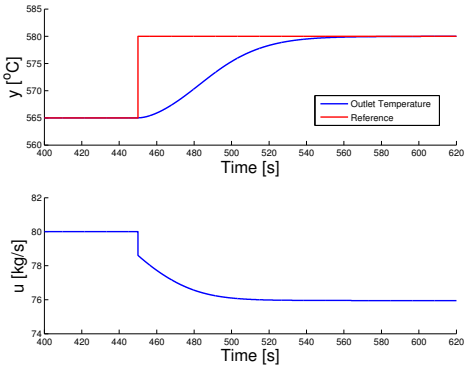

Figure 4.6: PI controlled system response to a reference step of 15^oC from nominal operating condition.

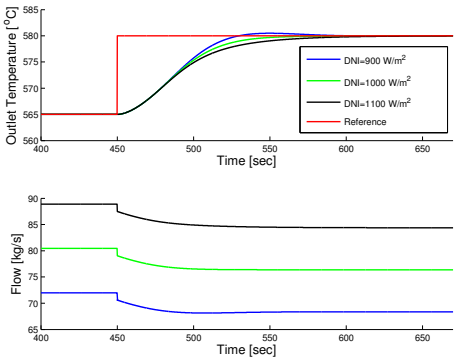

Figure 4.7: PI controlled system response to a reference step of 15^oC for different DNI.

Figure 4.8 shows the controlled system response obtained by a DNI step reduction of 60 W/m^2. The outlet temperature is reduced to $T = 552.8^oC$ and takes approximately 94s to recover to the nominal operating condition.

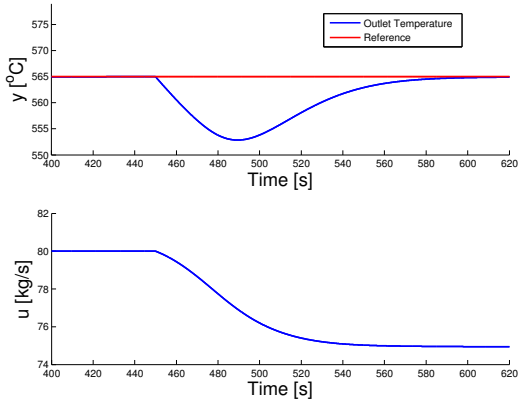

Figure 4.8: PI controlled system response to a step reduction of 60 W/m^2 from nominal DNI .

4.1.2 Gain-Scheduled PI Control

The GS is a control strategy for nonlinear systems in which the controller gains are automatically adjusted as a function of the scheduling variable. In this work, the dependent variable is the outlet temperature and the controller parameters are determined for working conditions of $T = 565\ ^oC$, $T = 550\ ^oC$, $T = 535\ ^oC$ and $T = 505\ ^oC$. The above mentioned functions are found by linearising the dependent variable over T. In order to determine the PI controller parameters for each operating condition, it is necessary to adapt the hysteresis relay limit values at the procedure stated in subsection 4.1.1. Figure 4.9 illustrates the GS scheme applied.

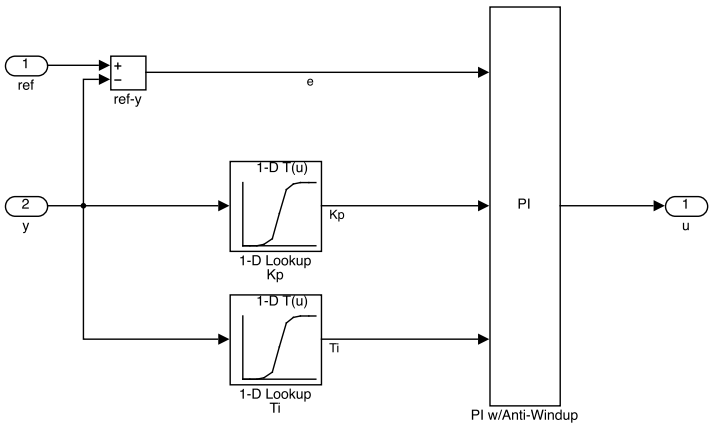

Figure 4.9: GS PI controller scheme.

The manipulated and controlled variable obtained by applying the aforementioned GS scheme is shown in figure 4.10. The outlet temperature tracks the reference signal for the temperature range.

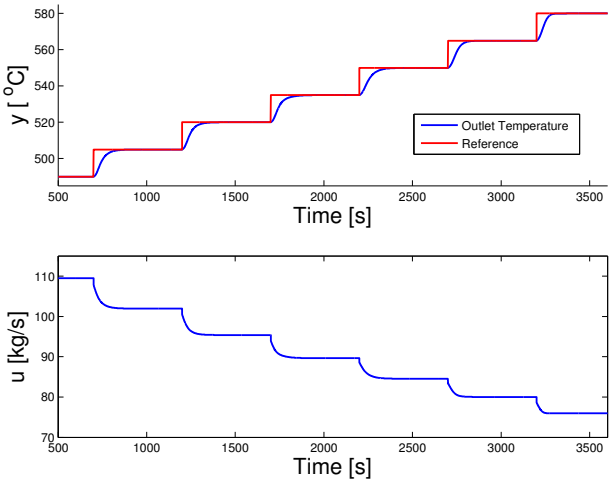

Figure 4.10: GS PI controlled system response to reference steps of $\delta T = 15^{o}C$, through different operating conditions.

4.2 LQG Control

The optimal controller presented is developed through a state-space approach and is applied to the discrete linear model identified in section 3.2. Such control system generates the manipulated variable by minimizing a quadratic cost function that yields a control signal given by a state feedback law.

The inability to measure the process states demand for a Linear Quadratic Estimator (LQE) coupled with the Linear Quadratic Regulator (LQR). The use of a Kalman filter as an estimator gives rise to the Linear Quadratic Gaussian (LQG) controller. The LQR and LQE are designed considering the separation principle that express the possibility to design the controller and the estimator separately without leading to any change in the closed loop poles of the LQG controller, for linear state-space systems [4]. Moreover, the resulting LQG system is always stable for a single-input single-output processes [4].

4.2.1 LQR

The LQR is a control system that aims to track a given constant value, in the presence of perturbations. Since only deviations from the operating condition are considered, the former controller reference is the derivative of a constant value thus, $r(k) = 0$. The optimal regulator is designed for linear time-invariant state-space system with a noise free structure given by,

$$\begin{aligned} x(k+1) &= Ax(k) + Bu(k) \\ y(k) &= Cx(k), \end{aligned} \tag{4.6}$$

where $k \in \mathbb{R}$ denotes discrete time, $x \in \mathbb{R}^n$ is the state vector, $u \in \mathbb{R}^m$ is the input vector, $y \in \mathbb{R}^p$ is the output vector, $A \in R^{n \times n}$ is the sate matrix, $B \in \mathbb{R}^{n \times m}$ is the input matrix, and $C \in \mathbb{R}^{p \times n}$ is the

output matrix.

The linear system is controllable and observable if the controllability matrix [4],

$$C(A,B) = [B\, AB\, A^2B \ldots A^{n-1}B], \tag{4.7}$$

and the observability matrix,

$$O(A,C) = \begin{bmatrix} C \\ CA \\ CA^2 \\ \vdots \\ CA^{n-1} \end{bmatrix}, \tag{4.8}$$

have full rank n. The examination of such matrices allows to conclude that the system is controllable and observable.

The control law that minimizes the optimal control infinite horizon quadratic cost function [4],

$$J = \frac{1}{2}\sum_{k=1}^{\infty}\Big[x^\top(k)Qx(k) + u^\top(k)Ru(k)\Big], \tag{4.9}$$

is given by,

$$u(k) = -k_{LQ}x(k). \tag{4.10}$$

where $Q \in \mathbb{R}^{n\times n}$ is a positive semi-definite matrix, $R \in \mathbb{R}^{m\times m}$ a positive definite matrix and k_{LQ} the feedback gain. The former variables weight the magnitude of the states and control signals, respectively. The use of $Q = C^\top C$ yields a cost function that ponders the input and output power through R, considering it is a scalar value. The increase of the latter parameter decreases the contribution of u and enhances y. Thus, the cost function can be written as,

$$J = \frac{1}{2}\sum_{k=1}^{\infty}\Big[y(k)^2 + Ru(k)^2\Big]. \tag{4.11}$$

The solution of the algebraic Riccati equation,

$$S = A^\top S[I + BR^{-1}B^\top S]^{-1}A + Q, \tag{4.12}$$

enables the calculus of the optimal gain,

$$K_{LQ} = (I + R^{-1}B^\top SB)^{-1}R^{-1}B^\top SA. \tag{4.13}$$

The LQR does not guarantee zero output steady-state error therefore, it is necessary to introduce the integral action that is represented by the following state,

$$x_I(k) = \frac{T_s}{q-1}e(k) \;\Leftrightarrow\; x_I(k+1) = x_I(k) + T_s e(k)\,, \tag{4.14}$$

where q is the forward shift operator, T_s is the sampling period and $e(k) = y(k) - r(k)$ is the error. The integral is connected in parallel with the control signal u, since it provides improved results than the series association. The complete state-space system is obtained by combining the plant linear model and integral states,

$$\begin{aligned} \bar{x}(k+1) &= \bar{A}\bar{x}(k) + \bar{B}u(k) \\ y(k) &= \bar{C}x(k), \end{aligned} \tag{4.15}$$

in which,

$$\bar{x} = \begin{bmatrix} x \\ x_I \end{bmatrix}, \quad \bar{A} = \begin{bmatrix} A & \underline{0} \\ -T_s C & I \end{bmatrix}, \quad \bar{B} = \begin{bmatrix} B \\ \underline{0} \end{bmatrix}, \quad \bar{C} = \begin{bmatrix} C & \underline{0} \end{bmatrix}$$

where $I \in \mathbb{R}^{p \times p}$ is the identity matrix.

The augmented system is controllable but not observable. Such problem is overcome by using the identified and augmented system. The first is used to observe and determine the plant model state feedback gain, whereas the second is used to determine the integral state feedback gain, since x_I does not need to be observed. In order to calculate the latter gain, it is necessary to modify the quadratic cost function,

$$J = \frac{1}{2} \sum_{k=1}^{\infty} \left[x^\top(k) Q x(k) + x_I^\top(k) Q_I x_I(k) + u^\top(k) R u(k) \right]. \tag{4.16}$$

where $Q_I \in \mathbb{R}^{p \times p}$ is chosen to be the identity matrix. The combination of the state variables into one vector leads to the rearranged quadratic cost,

$$J = \frac{1}{2} \sum_{k=1}^{\infty} \left[\bar{x}^\top(k) \bar{Q} \bar{x}(k) + u^\top(k) R u(k) \right], \tag{4.17}$$

in which,

$$\bar{x} = \begin{bmatrix} x \\ x_I \end{bmatrix}, \quad \bar{Q} = \begin{bmatrix} Q & \underline{0} \\ \underline{0} & I \end{bmatrix}. \tag{4.18}$$

The feedback control law is now given by,

$$u(k) = -\begin{bmatrix} K_x & K_I \end{bmatrix} \begin{bmatrix} x(k) \\ x_I(k) \end{bmatrix}. \tag{4.19}$$

where

$$\bar{S} = \bar{A}^\top \bar{S} [I + \bar{B} R^{-1} \bar{B}^\top \bar{S}]^{-1} \bar{A} + \bar{Q}, \tag{4.20}$$

and,

$$\begin{bmatrix} K_x & K_I \end{bmatrix} = (I + R^{-1} \bar{B}^\top \bar{S} \bar{B})^{-1} R^{-1} \bar{B}^\top \bar{S} \bar{A}. \tag{4.21}$$

The block diagram of the LQR controller applied to the augmented system is illustrated in figure 4.11.

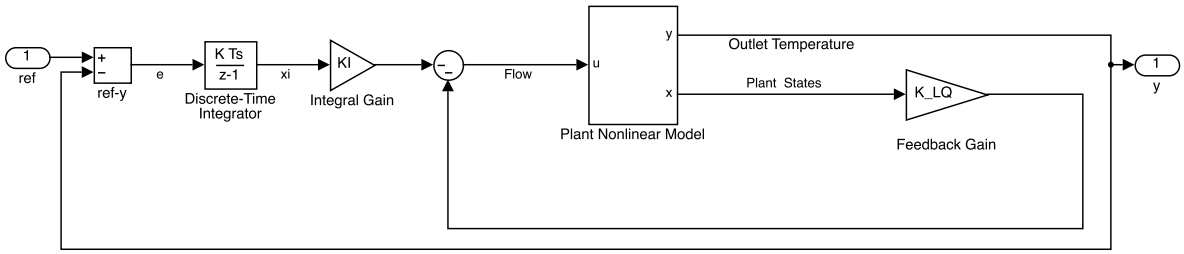

Figure 4.11: Block diagram of the LQR controller applied to the augmented system.

4.2.2 Kalman Filter

The discrete linear model states need to be estimated in order to use the optimal regulator developed in section 4.2.1. This aim is achieved by considering the following model structure,

$$x(k+1) = Ax(k) + Bv(k) + Gw(k)$$
$$y(k) = Cx(k) + v(k),$$

where $G \in \mathbb{R}^{n\times n}$ is the identity matrix. The process noise $w(k)$ and the measurement noise $v(k)$ are uncorrelated Gaussian sequences with zero mean and covariance given by,

$$Q_n = E[w(k)w^\top(k)]\,, \qquad R_n = E[v(k)v^\top(k)]\,.$$

The Kalman filter is a state estimator that minimizes the estimation error covariance,

$$J_o = E\sum_{k=1}^{\infty}\left[||x(k) - \hat{x(k)}||^2\right]. \tag{4.22}$$

In other words, it optimizes the signal-to-noise ratio of a model with Gaussian disturbances. The minimization of equation (4.22) that leads to a centred estimator yields a dynamic system that uses the input and output measurements to determine the state estimate. The latter is called an observer and can be developed using the most recent observation,

$$\hat{x}(k|k) = A\hat{x}(k-1|k-1) + Bu(k-1) + M\big[y(k) - C\hat{x}(k|k)\big]. \tag{4.23}$$

The Kalman filter gain that minimizes the cost function (4.22) is given by,

$$M = PC^\top(CPC^\top + R_n)^{-1}, \tag{4.24}$$

where the covariance of the estimation error matrix P satisfies the algebraic Riccati equation,

$$P = A^\top P[I + BR_n^{-1}B^\top P]^{-1}A + Q_n. \tag{4.25}$$

The block diagram of the LQG controller applied to the augmented system is illustrated in figure 4.12.

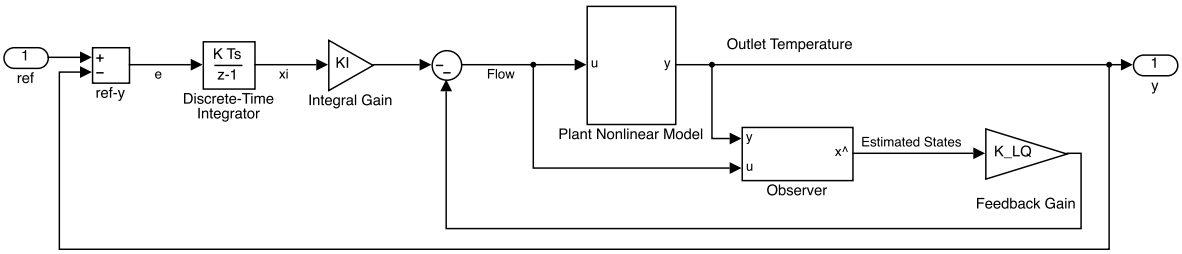

Figure 4.12: Block diagram of the LQG controller applied to the augmented system.

4.2.3 LQG Controller Design

The plant LQG controller is completely designed after tuning the weighting parameters R, R_n and Q_n that influence the optimal controller and observer pole placement.

Figures 4.13 and 4.14 illustrate the overshoot percentage, $S(\%)$, and rise time, T_r, of the outlet temperature to a reference step of $\delta T = 15^oC$ as a function of R, and the step response to several values of the control action weighing parameter, respectively. As R decreases, the time response diminishes while the overshoot rises. It can be seen that the growth of the input signal power leads to the appearance of oscillatory behaviour. The value of R is designed in order to minimize the outlet temperature response rise time while maintaining a reduced overshoot and valve oscillation. Such consideration yields a weighting parameter of $R = 2.8 \times 10^{14}$ for $T_r \approx 94.22\ s$ and $S(\%) \approx 0.0372$.

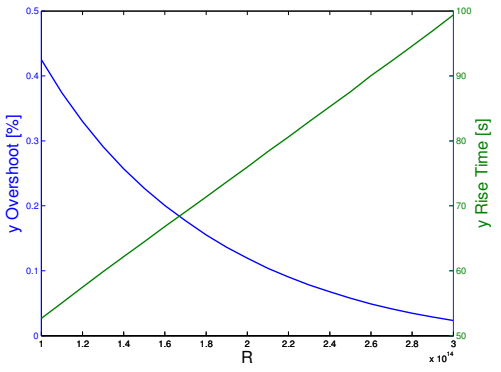

Figure 4.13: Overshoot percentage relative to the final value and rise time of the outlet temperature to a reference step of $\delta T = 15^oC$, as a function of R.

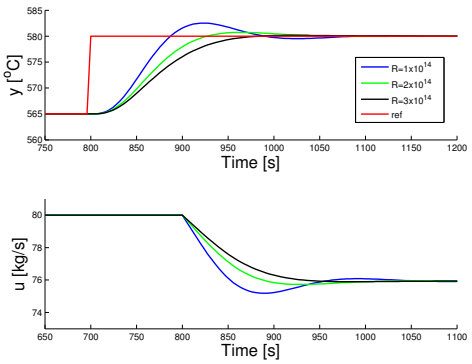

Figure 4.14: Output response to a reference step of $\delta T = 15^oC$ for several values of R.

Figure 4.15 illustrate the same signals for different DNI. The maximum temperature value, $T_{max} = 580.8^oC$, is obtained for DNI=900 W/m^2. As in the case of the PI controller, the system response overshoot change due to different DNI amplitude is minimum.

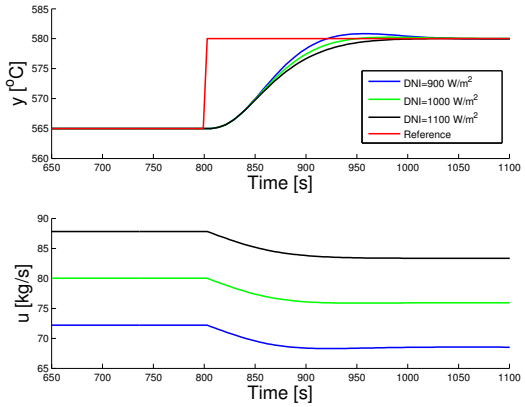

Figure 4.15: LQG controlled system response to a reference step of 15^oC for different DNI.

Figure 4.16 shows the controlled system response obtained by a DNI step reduction of 60 W/m^2. The outlet temperature is reduced to $T = 549.4^oC$ and recovers to the nominal operating condition within a time interval of approximately 160 s.

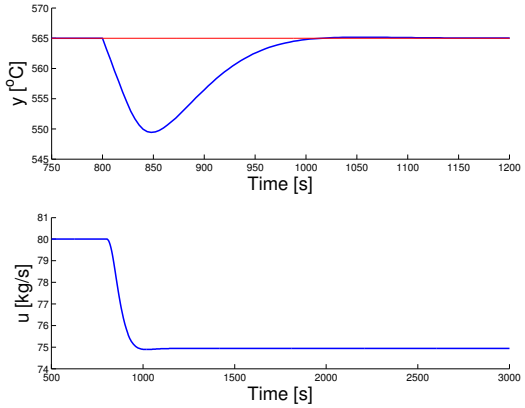

Figure 4.16: LQG controlled system response to a step reduction of 60 W/m^2 from nominal DNI.

The gain margin, G_M, and phase margin, P_M, are generally reduced by the Kalman filter, which worsens the controlled system relative stability. In order to approximate the stability indicators of the LQG to the LQR controller, a Loop Transfer Recovery (LTR) is conducted by adjusting the covariance matrices R_n and Q_n. Considering the linear state space system and the feedback control law given by equation (4.6), the open loop transfer function of the LQR applied to the process is obtained,

$$P(Z) = -K_{LQ}(ZI - A)^{-1}B. \tag{4.26}$$

Using equations (4.23), the Kalman filter dynamic compensator transfer function can be determined,

$$C(Z) = -K_{LQ}(ZI - A + BK_{LQ} + MCA - MCBK_{LQ})^{-1}M. \tag{4.27}$$

Assuming $Q_n = BB'$, the LTR is performed by increasing the covariance matrix R_n. As the latter variable rises, the gain and phase margins become more approximate do the LQR. Moreover, for

higher values of R_n, the gain margin of the LQG controller becomes superior than the LQR. Table 4.2 details the relative stability indicators for a designed value of $R_n = 1 \times 10^{17}$.

Table 4.2: Relative stability indicators for the LQR and LQG controllers, using $R_n = 1 \times 10^{17}$ and $Q_n = BB'$.

		Margin	Frequency $[\omega]$
LQ	$G_m^{LQ}[db]$	104.1	0.79
	$P_m^{LQ}[^o]$	∞	-
LQG	$G_m^{LQG}[db]$	218.73	0
	$P_m^{LQG}[^o]$	∞	-

4.2.4 Multi-Model Adaptive LQG Control

The multi-model adaptive LQG controller consists of a parallel association of a set of controllers designed for different operating temperatures, as shown in figure 4.17. For each working condition, only one controller contributes to the control signal whereas in the transition between operating points, it results from the output combination of the two controllers involved. The signals are weighted by temperature dependent functions.

The presented control scheme tracks the reference signal however, overshoots at the outlet temperature are verified between controller transitions. The undesired 'bumps' are due to the control systems output difference at the switching instant, since the LQG controllers are based on different models and the temperature dependent functions cannot handle the transition for every temperature. The aforementioned problem is overcome through bumpless transfer.

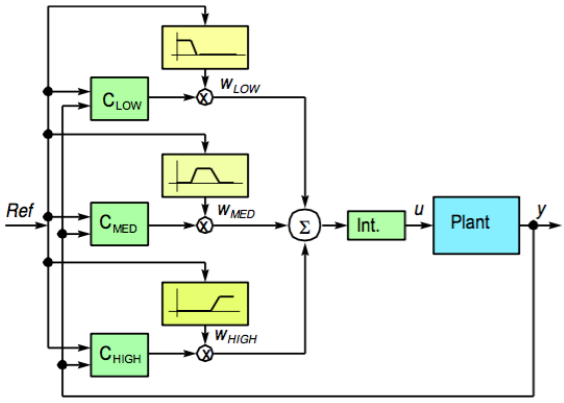

Figure 4.17: Multi-model adaptive control scheme.

4.2.4.A Bumpless Transfer

The transient behaviour during switching is minimized by initializing the integrator state of the future on-line controller C^F. The initialization compensates the difference between the valve position given by the current controller C^C and the control contribution generated by the feedback system of C^F. The integral state is obtained by rearranging the following expression,

$$u(k) = -\begin{bmatrix} K_{LQ} & K_I \end{bmatrix} \begin{bmatrix} x(k) \\ x_I(k) \end{bmatrix}. \tag{4.28}$$

Thus, the future on-line controller C^F initial integral state is given by,

$$x_I^F(k) = -{K_I^F}^{-1}\big[u(k)^C + K_{LQ}^F \hat{x}^F(k|k)\big]. \tag{4.29}$$

where $u(k)^C$ is the current valve position. Figure 4.18 illustrates the controlled system response obtained by initializing the integral state while using the multi-model adaptive scheme. It can be concluded that no overshoot is visible at any changing instant. Figure 4.19 shows the same experiment in the absence of the adaptation structure. Although the controller tracks the reference, the performance is unsatisfactory for operating temperatures different from the nominal regime.

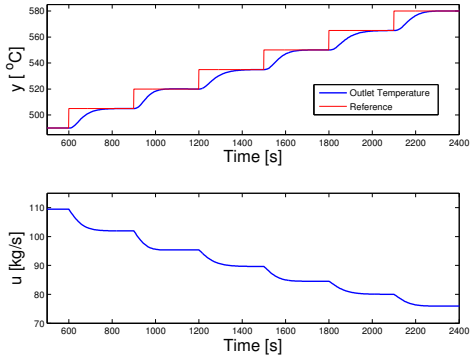

Figure 4.18: Multi-model adaptive LQG controller with bumpless transfer controlled and manipulated variables obtained for reference steps of $\delta T = 15^oC$, through different operating conditions.

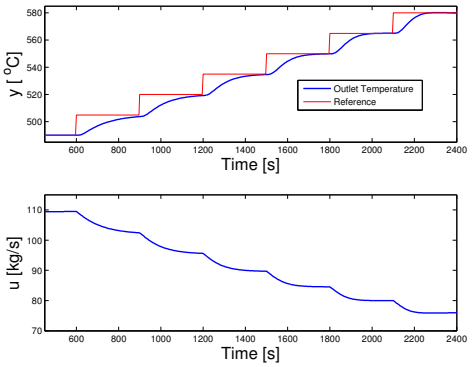

Figure 4.19: LQG controlled system response to reference steps of $\delta T = 15^oC$, through different operating conditions.

4.3 Feed-forward Control

The static feed-forward controller developed aims to reject a measured disturbance with a control signal u_{ff} that is proportional to the perturbation. In this work, the external signal is given by the difference between the average incident and nominal DNI. Figure 4.20 illustrate the feed-forward controller applied to the plant,

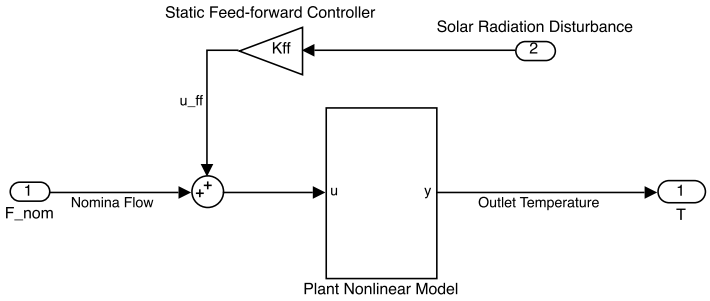

Figure 4.20: Block diagram of the static feed-forward controller applied to the nonlinear plant.

The control action results from,

$$u_{ff} = K_{ff}\delta I, \tag{4.30}$$

where the controller gain K_{ff} is chosen so that the valve position given by the feedback controller is added with u_{ff}, in order to compensate the outlet temperature deviation caused by the average solar radiation change δI. The gain is positive since the manipulated variable must change accordingly with the sign of the perturbation. Figure 4.21 shows the outlet temperature deviation caused by a disturbance of $\delta I = 60W/m^2$, considering nominal working conditions. The steady-state error is eliminated by a static feed-forward controller with $K_{ff} = 1.3851 \times 10^{-6}$, that reduces the maximum value of the plant output to $T = 566.4^oC$, as illustrated in figure 4.22. Furthermore, figure 4.23 shows that the developed controller is valid for different amplitude values of the aforementioned perturbation.

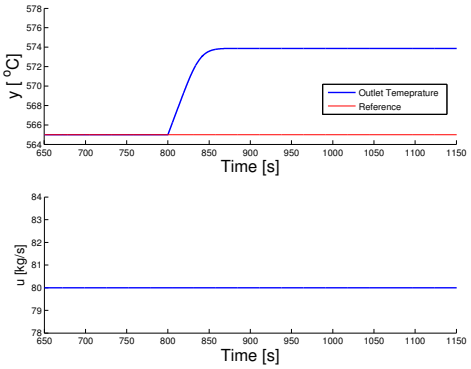

Figure 4.21: Outlet temperature deviation due to an increase of DNI by 60 W/m^2.

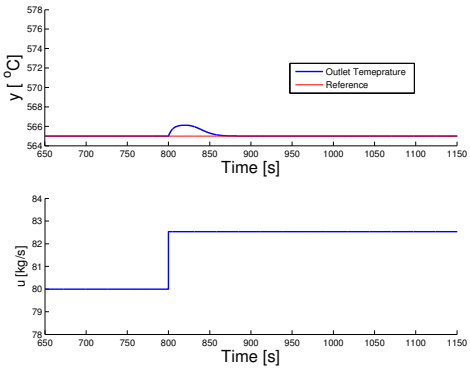

Figure 4.22: Outlet temperature response of the feed-forward controlled process due to an increase of DNI by 60 W/m^2.

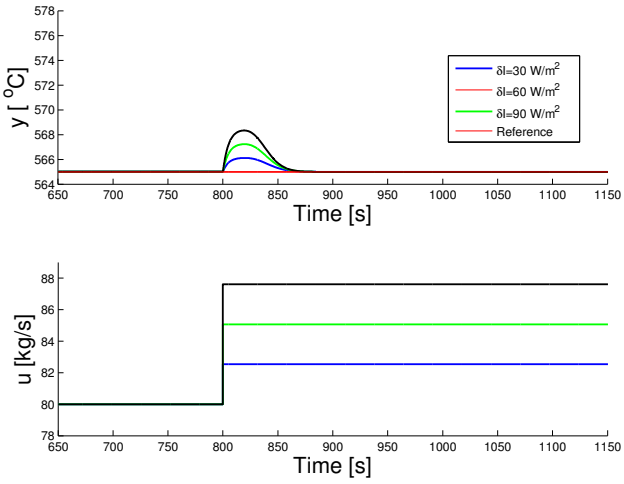

Figure 4.23: Outlet temperature response and the manipulated variable obtained by perturbing the process with different magnitudes of DNI.

The nonlinear temperature dynamics demand for a changing static feed-forward controller. The latter is determined by a quadratic fitting of the static gain as a function of the outlet temperature, for working temperatures of $T_{out} = 505^oC$, $T_{out} = 520^oC$,$T_{out} = 535^oC$, $T_{out} = 550^oC$ and $T_{out} = 565^oC$,

$$K_{ff} = 2.625 \times 10^{-11}T - 2.187 \times 10^{-8}T + 5.735 \times 10^{-6}. \tag{4.31}$$

4.4 Predictive Adaptive Control

An adaptive controller uses a scheme for automatic adjustment of the controller gains in real time, so that the performance of the control system is maintained when the process dynamics change. In this work, the former approach is achieved with the Multistep Multivariable Adaptive Regulator (MUSMAR) control algorithm that is based on Model Predictive Control (MPC). In order to obtain a steady-state solution approximate to the optimal control problem, MUSMAR predictors are used.

4.4.1 Model Predictive Control

The MPC is a controller design concept in which the manipulated variable is determined at the beginning of every sample period by minimizing a multistep cost function defined along an horizon of future discrete time instants such as [3],

$$J_{T_P} = \varepsilon\Big\{\Sigma_{j=1}^{T_P}\tilde{y}^2(k+j) + \rho\Sigma_{j=1}^{T_u}\hat{u}^2(k+j-1)|I^k\Big\}, \tag{4.32}$$

where $\varepsilon[.|I^k]$ is the mean of the information available up to time k, T_P is the prediction horizon, T_u is the control horizon and ρ is the virtual manipulated variable $\hat{u}$ penalty term. The tracking error is given by

$$\tilde{y}(k) = y(k) - r^*(k), \tag{4.33}$$

in which $y(k)$ is the measured output and $r^*(k)$ is the virtual reference that connects the present value of y with the desired value at the end of the prediction horizon, $r(k+T)$ [3].

The minimization of equation (4.32) is accomplished by describing the plant dynamics through predictive models that relate the samples of the manipulated variable and the predicted values of the plant output within the prediction horizon [3]. The former optimization yields a sequence of $\hat{u}$, in which only the first is applied to the plant.

4.4.2 MUSMAR Predictors

The MUSMAR predictive models are developed by constraining the manipulated variable u to be a constant feedback of the pseudo-state s, along an horizon from $k+1$ up to $k+T_P-1$ [3]. The predictors for the output and future values of the control samples are given by,

$$\hat{y}(k+j|k) = \theta_j u(k) + \psi_j' s(k), \tag{4.34}$$

and,

$$\hat{u}(k+j|k) = \mu_j u(k) + \phi_j' s(k), \tag{4.35}$$

respectively. The symbols $\theta_j \,\epsilon\, \mathbb{R}^{n_s}$, $\psi_j \,\epsilon\, \mathbb{R}^{n_s}$, $\mu_j \,\epsilon\, \mathbb{R}^{n_s}$ and $\phi_j \,\epsilon\, \mathbb{R}^{n_s}$ are parameters estimated from plant data using least squares and n_s is the dimension of s. The pseudo-state variable can include feed-forward terms from accessible disturbances, or measurable state variables [3].

4.4.3 MUSMAR Algorithm

The MUSMAR algorithm determines the manipulated variable through the following procedure [3]:

1.Determine the tracking error $\tilde{y}$ through equation (4.33), by sampling the plant output y.

2.Update the estimates of the parameters θ, ψ, μ and ϕ using RLS with directional forgetting.

3.Determine the controller gains vector,

$$F = -\frac{1}{\alpha}\Big(\sum_{j=1}^{T_P}\theta_j\phi_j + \rho\sum_{j=1}^{T_P-1}\mu_j\phi_j\Big), \tag{4.36}$$

where $\alpha > 0$ is the normalization factor given by,

$$\alpha = \sum_{j=1}^{T_P}\theta_j^2 + \rho\Big(1 + \sum_{j=1}^{T_P-1}\mu_j^2\Big). \tag{4.37}$$

3. Apply the control signal,

$$u(t) = F's(t) + \eta(t), \tag{4.38}$$

in which η is the white dither noise of small amplitude.

Figure 4.24 illustrate the MUSMAR structure. The controller gains are adapted after the estimation of the predictive models parameters.

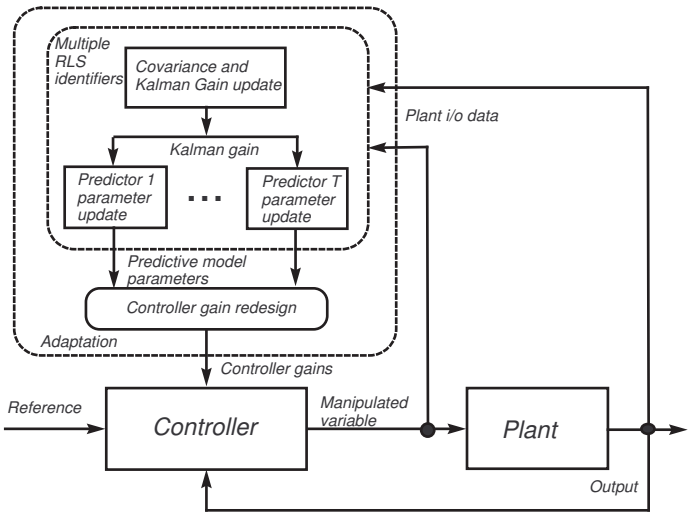

Figure 4.24: MUSMAR structure [3].

4.4.4 Dynamic Cost

The MUSMAR controller action can be improved if dynamic weights are incorporated at the cost function given by equation (4.32). In this way, the controlled system has a superior tracking capability since the controller becomes more robust to plant anti-resonance characteristics. Considering the filtered variables [3],

$$y_H(k) = H(q)y(k), \tag{4.39}$$

and,

$$\hat{u_H}(k) = H(q)\hat{u}(k), \tag{4.40}$$

the new cost function is determined,

$$J_{T_P} = \varepsilon\Big\{\Sigma_{j=1}^{T_P}\Big(H(q)y(k+j) - r*(k+j)\Big)^2 + \rho\Sigma_{j=1}^{T_u}\Big(H(q)\hat{u}(k+j-1)\Big)^2|I^k\Big\}, \tag{4.41}$$

Hence, the control signal applied to the plant results from,

$$u(k) = \frac{1}{H(q)}u_H(k) \tag{4.42}$$

where $u_H(k)$ is the manipulated variable given by the MUSMAR control algorithm.

4.4.5 Solar Tower Predictive Adaptive Control

The predictive adaptive controller parameters are selected in order to enhance the controlled system performance. Table 4.3 details the initial values used.

Table 4.3: Initial parameters used for the MUSMAR controller configuration process.

Description	Symbol	Value
Sampling period	T_s	0.1 s
Forgetting factor	λ	0.995
Number of states in the pseudo-state of the output	n_a	10
Number of states in the pseudo-state of the input	n_b	4
Number of states in the pseudo-state of the reference	n_g	1
Manipulated variable penalty term	ρ	1000
Dither noise	η	1×10^{-5}

The prediction horizon is chosen so that the cost function given by,

$$J = \frac{1}{N}\Big[\sum_{k=1}^{N}(y(k) - r(k))^2 + \rho\sum_{k=1}^{N}u(k-1)^2\Big], \tag{4.43}$$

is minimum. Figure 4.25 illustrate the steady state cost (4.43) dependence on T_P. As the prediction horizon increases, the dependent variable decreases since the cost becomes approximate to the infinite horizon solution. The opposite is verified for $T_P > 12$ due to the predictors degradation. For $T_P = 1$ the predictor is able to track the reference although, the cost is high. The value chosen for the prediction horizon is $T_P = 9$ since high quality results are obtained.

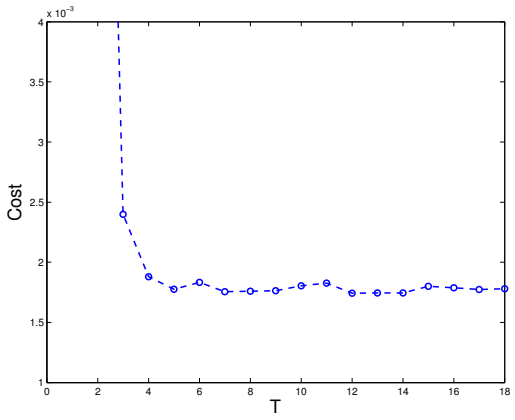

Figure 4.25: The steady state cost (4.43) as a function of the prediction horizon.

The results hereafter presented are obtained by filtering the desired outlet temperature with the following first order system

$$M(s) = \frac{1}{T_d s + 1}, \tag{4.44}$$

where $T_d = 12s$ is the filter time constant. In this way, the reference changes are less abrupt.

The outlet temperature and flow command of the controlled system to a reference step of $\delta T = 15^o C$ is illustrated in figure 4.26. The manipulated variable has undesirable high frequency oscillations due to plant high frequency anti-resonance modes. The obtained control signal diminishes the actuator lifetime and so, it is necessary to incorporate a dynamic weight in MUSMAR. The latter is considered to be a high pass filter given by,

$$H(q) = \frac{1 - \alpha q^{-1}}{1 - \alpha}, \tag{4.45}$$

where α is a constant value that *locus* the zero of the filter in the frequency domain. Figure 4.27 illustrate the controlled system response obtained by using a dynamic weight with $\alpha = 0.9$. It can be seen that the removal of high frequency oscillations at the MUSMAR control signal reduces the wear of the actuator.

Also, the manipulated variable penalty term needs to be increased in order to reduce the control signal power, avoiding the lower frequency oscillation. The rise of ρ leads to the appearance of an offset that is extinguished by using an integrator associated in parallel with the MUSMAR control signal. Figure 4.28 illustrate the controlled system response to a reference step of $\delta T = 15^o C$, obtained with the modified parameters detailed in table 4.4. The outlet temperature tracks the reference without the existence of peaks or oscillatory behaviour at the manipulated and controlled variable. The outlet temperature has a rise time of approximately 131 s in the absence of overshoot. Figure 4.29 show the MUSMAR gains changing as the system dynamics modify.

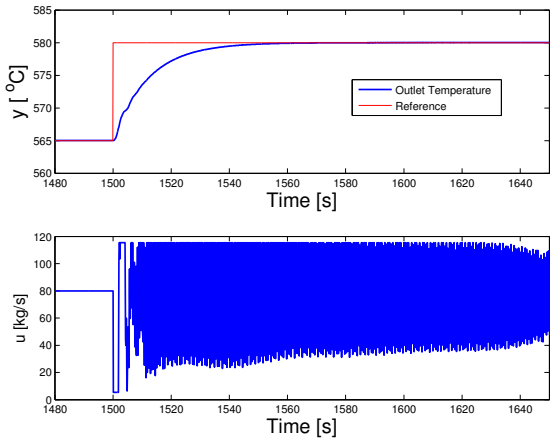

Figure 4.26: MUSMAR controlled system response to a reference step of $\delta T = 15^oC$ with the parameters detailed in table 4.3.

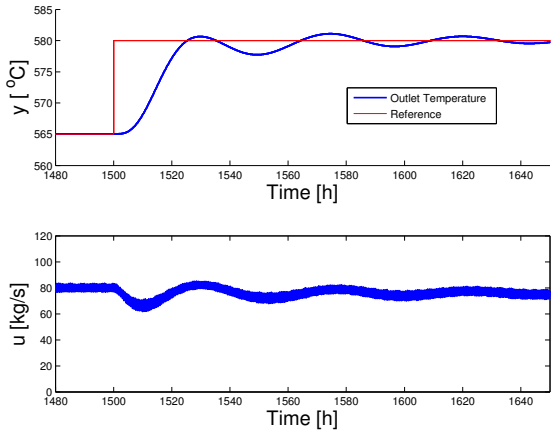

Figure 4.27: MUSMAR controlled system response to a reference step of $\delta T = 15^oC$ with the parameters detailed in table 4.3, in the presence of a dynamic weight with $\alpha = 0.9$.

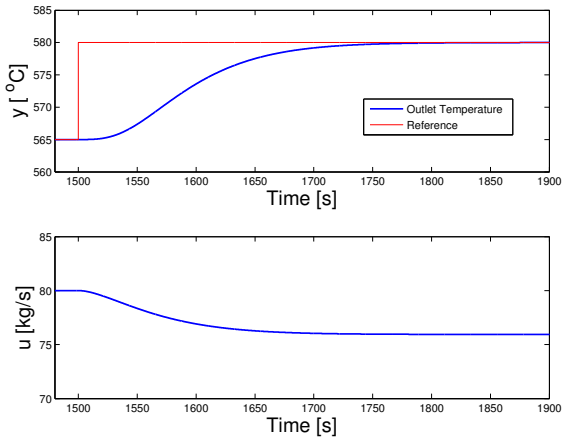

Figure 4.28: MUSMAR with integral action controlled system response to a reference step of $\delta T = 15^oC$ with the modified parameters detailed in table 4.4.

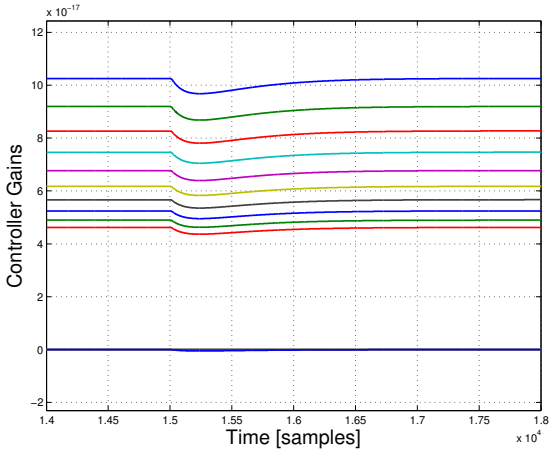

Figure 4.29: MUSMAR controller with integral action gains adaptation to a different operating condition.

Table 4.4: Final configuration of the MUSMAR controller with integral action.

Description	Symbol	Value
Dynamic weight filter zero	α	0.9
Reference filter time constant	T_d	12 s
Integral gain	K_I	-5×10^{-8}
Penalty term	ρ	8×10^6
Dither noise	η	1×10^{-17}

Figure 4.30 illustrate the controlled system response to a DNI step reduction of 60 W/m^2. The outlet temperature is reduced to $T = 549.6^oC$ and takes approximately 200s to return to the nominal operating condition.

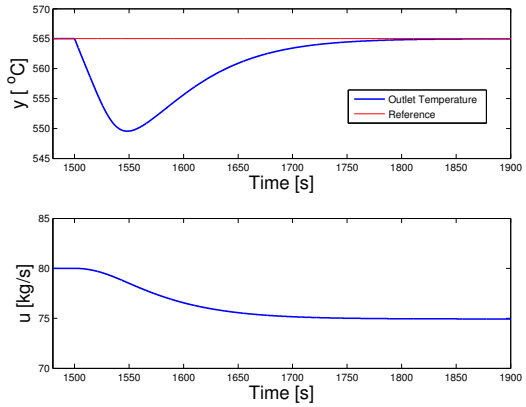

Figure 4.30: MUSMAR controlled system response to a DNI step reduction of 60 W/m^2.

Figure 4.31 show the outlet temperature tracking the reference through different operating conditions. The controlled variable follows the set-point for the temperature range.

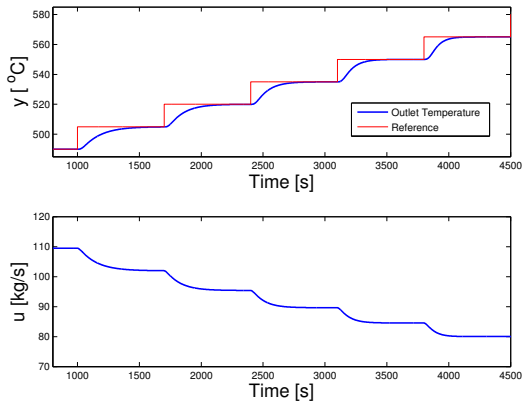

Figure 4.31: The outlet temperature and flow command of the MUSMAR with integral action controlled system through different operating conditions.

4.5 Coordinated Control

The coordinated control strategy is a mean to maintain the outlet temperature at a desired set-point by manipulating the fluid flow and the radiation flux of the east and west side of the heliostat field, as illustrated in figure 4.32. Each mirror region dynamics is considered to be a first order system with a time constant of $T_h = 4/3s$ that is related with the time required to refocus the mirrors. The manipulated variable is the heliostat field area that is given by a PI controller with anti-windup wherein its parameters are design to achieve a step response time of approximately 4 s. The valve controller has the specifications stated in section 2.2. The same control concept is used for the outlet temperature controller.

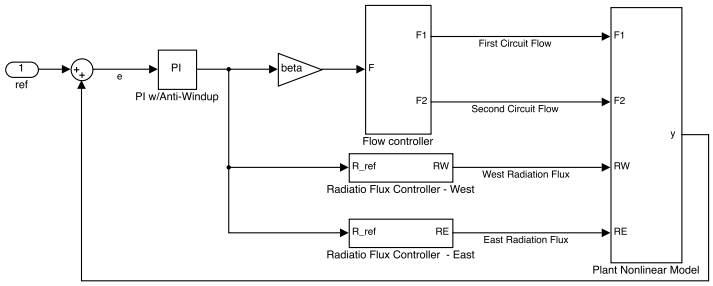

Figure 4.32: Coordinated control scheme.

The variable β is chosen as the ratio between the nominal flow and radiation flux reflected by the heliostat field,

$$\beta = \frac{F_{nom}}{R}. \tag{4.46}$$

The outlet temperature PI controller parameters are determined through trial and error while considering constant DNI over the heliostat field for all panels. The flow control signal has a reverse action and represents the increment relative to the nominal operation. Figure 4.33 shows the controlled system response to a reference step of $\delta T = 15^oC$ from nominal operating condition. In order to track the desired outlet temperature, the flow is reduced and the radiation flux is increased. For higher values of β the flow and radiation flux are superior. The output variable has no overshoot and a rise time of approximately 107 s.

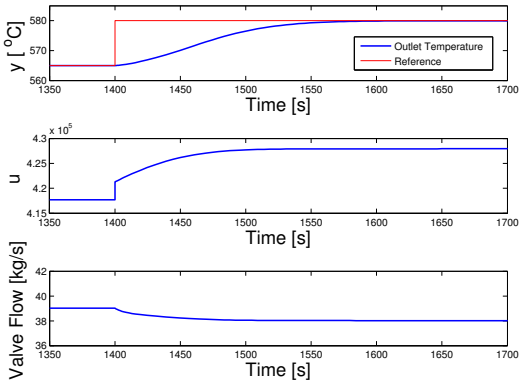

Figure 4.33: The outlet temperature controller manipulated and controlled variable, and the valve output flow.

Figure 4.34 shows the controlled system response due to a DNI step reduction of 60 W/m^2. The outlet temperature only decreases to $T = 559.1^oC$ and recovers to the nominal operating condition within a time interval of approximately 155 s.

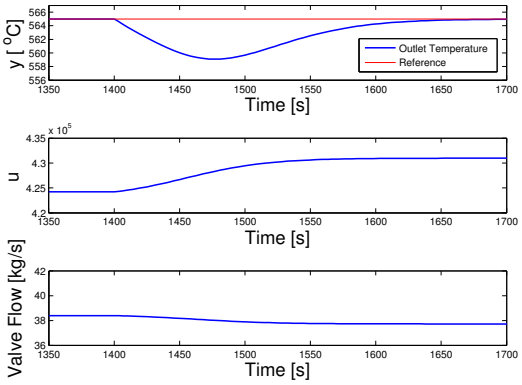

Figure 4.34: Coordinated controlled system response to a step reduction of 60 W/m^2 from nominal DNI.

4.5.1 Gain-Scheduled Coordinated Control

The GS scheme is now developed for the coordinated controller using the procedure presented in subsection 4.1.2. The scheduling variable is also the outlet temperature and the controller parameters are determined for working conditions of $T = 565\ ^oC$, $T = 535\ ^oC$ and $T = 505\ ^oC$. The constant β is kept constant. Figure 4.35 illustrate the use of the GS scheme with coordinated control. The outlet temperature tracks the reference signal for the temperature range.

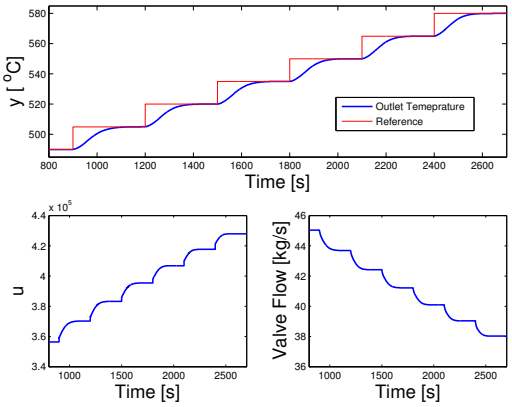

Figure 4.35: GS coordinated controlled system response for reference steps of $\delta T = 15^oC$, through different operating conditions.

5

Optimal Operation

Contents

The solar tower efficiency is addressed by taking considerations regarding the energy collecting system and the turbo-generator, that is modelled in conjunction with the Rankine cycle. The former system efficiency decreases as the temperature rises due to the increase of thermal losses while the EPGS efficiency increases with temperature. This trade-off leads to maximum power production for a given outlet temperature.

The optimal operation of a solar tower is achieved by considering a two-layer structure, as illustrated in figure 5.1. The first layer provides the outlet temperature set-point that optimizes the electrical production, whereas the second corresponds to the outlet temperature controller that has been developed in chapter 4. In this work, the maximum output power is desired and thus, the electrical production economical dispatch is not considered. The latter could be included in a higher hierarchical layer.

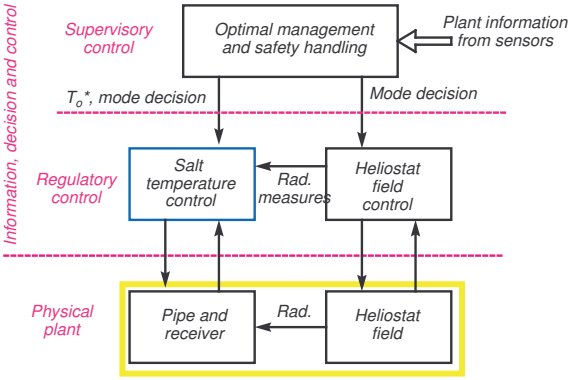

Figure 5.1: Optimal operation control system structure: The controlled solar tower as a cyber-physical system.

5.1 Static Optimization

The static optimization aims to determine the outlet temperature that leads to the highest power production of the solar plant by examine the system equilibrium operation. Thus, all the variables and parameters are considered to be constant. The analysis of the overall plant performance is divided in power collection, thermal storage and electrical power production systems.

5.1.1 Power Collection

The heliostat field and the receiver comprises the energy collection system. The solar power gathered by the mirrors that is focused on the heat exchanger results from,

$$P_{inc} = \eta_{hel} I S, \qquad \text{[W]} \quad (5.1)$$

where is S the total heliostat reflective area, I is the DNI and η_{hel} is a constant parameter that accounts for field availability and mirrors reflectivity, cleanliness and efficiency. The average radiation flux focused at the receiver is given by,

$$R = \frac{P_{inc}}{A_{rec},} \qquad \text{[W m}^{-2}\text{]} \quad (5.2)$$

where A_{rec} is the heat exchanger area.

The flow required to achieve a given outlet temperature can be determined using a concentrated parameter model for each receiver tube $j = 1, ..., n_t$,

$$\frac{T_j}{dt} = -F_j\Big(\frac{T_j - T_{in}}{L}\Big) + \alpha R - \gamma\Big(\frac{T_j - T_{in}}{2} - Ta\Big). \tag{5.3}$$

where n_t is the total amount of tubes.

In equilibrium the temperature time derivative is zero thus, the flow of each circuit, $i = 1, 2$, can be found,

$$F_i = n_t \frac{\alpha R - \gamma\Big(\frac{T_i - T_{in}}{2} - Ta\Big)}{\big(T_i - T_{in}\big)} L, \tag{5.4}$$

where L is the flow circuit length. The temperature dependent parameters are set for the average temperature of the fluid path.

The thermal power absorbed by the molten salt results from the contribution of both receiver circuits,

$$P_{coll} = \Sigma_{i=1}^{2} \dot{m}_i c_{f,i} \rho_{f,i} \big(T_i - T_{in}\big). \quad \text{[W]} \tag{5.5}$$

The receiver thermal losses are only considered to be temperature dependent and are obtained by receding from the Partial Differential Equation (PDE) to the energy conservation equation (3.1). Therefore, the concentrated parameter model for the thermal losses is given by,

$$P_{rl} = \Sigma_{i=1}^{2} \gamma T_{av,i} c_{f,i} \rho_{f,i} A_{cs} L n_t, \quad \text{[W]} \tag{5.6}$$

where T_{av} is the average temperature. The information regarding the collected power and losses allow the calculus of the receiver efficiency,

$$\eta_{rec} = \frac{P_{coll}}{P_{coll} + P_{rl}}. \tag{5.7}$$

Hence, the efficiency of the power collection system can be found,

$$\eta_{coll} = \eta_{hel} \eta_{rec}. \tag{5.8}$$

5.1.2 Thermal Storage

The receiver outlet fluid passes through a storage tank before being used. The thermal storage system has an energy delivery efficiency and heat losses to the environment that can be approximately described by the following temperature dependent function,

$$P_{tsl} = \sigma\big(T - T_a\big), \qquad \text{[W]} \quad (5.9)$$

where σ is a parameter obtained from tests performed at the tank. For simulation purpose, σ is designed for a storage thermal efficiency of 99,3% at nominal operation. The latter performance index is given by,

$$\eta_{st} = \frac{P_{salt}}{P_{coll}}, \qquad (5.10)$$

where $P_{salt} = P_{coll} - P_{tsl}$ is the Electrical Power Generating System (EPGS) input thermal power.

5.1.3 Electrical Power Production

The Solar Two EPGS is a Rankine cycle with an efficiency described by,

$$\eta_{Rank} = K\Big(1 - \frac{T_{cond}}{T}\Big). \qquad (5.11)$$

where $K \leq 1$ is a constant that models the performance loss with respect to the ideal Carnot cycle and T_{cond} is the Rankine condenser temperature [20].

The power consumption of the parasitic elements relative to the overall production is considered to be constant. In order to consider such loss, the net electrical power is affected by a weighting parameter η_p,

$$P_e = P_{salt}\eta_{Rank}\eta_p. \qquad \text{[W]} \quad (5.12)$$

The plant efficiency results from the product of the power collection, thermal storage and the electric power production systems,

$$\eta_{plant} = \eta_{coll}\eta_{Rank}\eta_{st}\eta_{np}. \qquad (5.13)$$

5.1.4 Optimal Temperature Set-point

The optimal outlet temperature reference is obtained by maximizing the net electrical power production subject to the maximum and minimum temperature and fluid flow,

$$max P_e(T) \qquad (5.14)$$

s.t.

$$\begin{cases} F_{1,2}^{min} \leq F_{1,2} \leq F_{1,2}^{max} \\ T^{min} \leq T \leq T^{max} \end{cases} \qquad (5.15)$$

5.2 Solar Tower Static Optimization

The static optimization algorithm is now analysed with the Solar Two CRS concentrated parameter model in order to study the outlet temperature set-point variation with parameters or disturbances. The fluid flow is considered to be equal for both paths and the solar radiation flux is constant and identical for all panels. Table 5.1 details the nominal values used for simulation purpose. The designated efficiencies are found through data collected from plant operation [1].

Table 5.1: Nominal values used for static optimization purpose of the Solar Two.

Description	Symbol	Value
Heliostat field efficiency	η_{hel}	0.53
Parasitic loads	η_p	0.87
Fluid circuit length	L	95.52 m
Thermal storage loss coefficient	σ	389.58 W/o^C
Rankine cycle performance index	K	0.355 kW/m^2
Condenser temperature	T_{cond}	21^oC

The effect of varying the DNI at the power collection, thermal storage, Rankine cycle and plant efficiency is illustrated in figure 5.2. The rise of DNI increases the incident power thus, the fluid flow to maintain the same outlet temperature is superior. This fact rises the collected energy and the ratio between the former and thermal losses which leads to a higher efficiency. For superior temperatures, the latter evidence is more significant and hence, the optimal outlet temperature is higher. The same behaviour is verified when the receiver or storage thermal loss coefficient is reduced, as shown in figure 5.3 and 5.4. The Rankine cycle efficiency is unchanged since it only depends on the outlet and condenser temperatures.

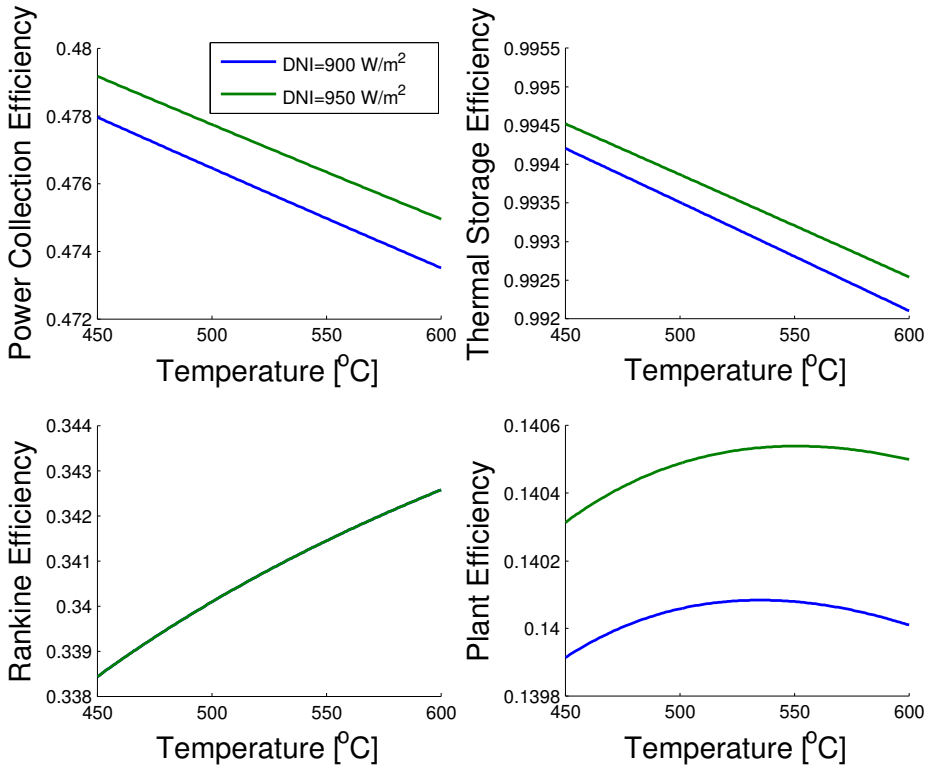

Figure 5.2: Power collection, thermal storage, Rankine cycle and overall plant efficiency for different DNI.

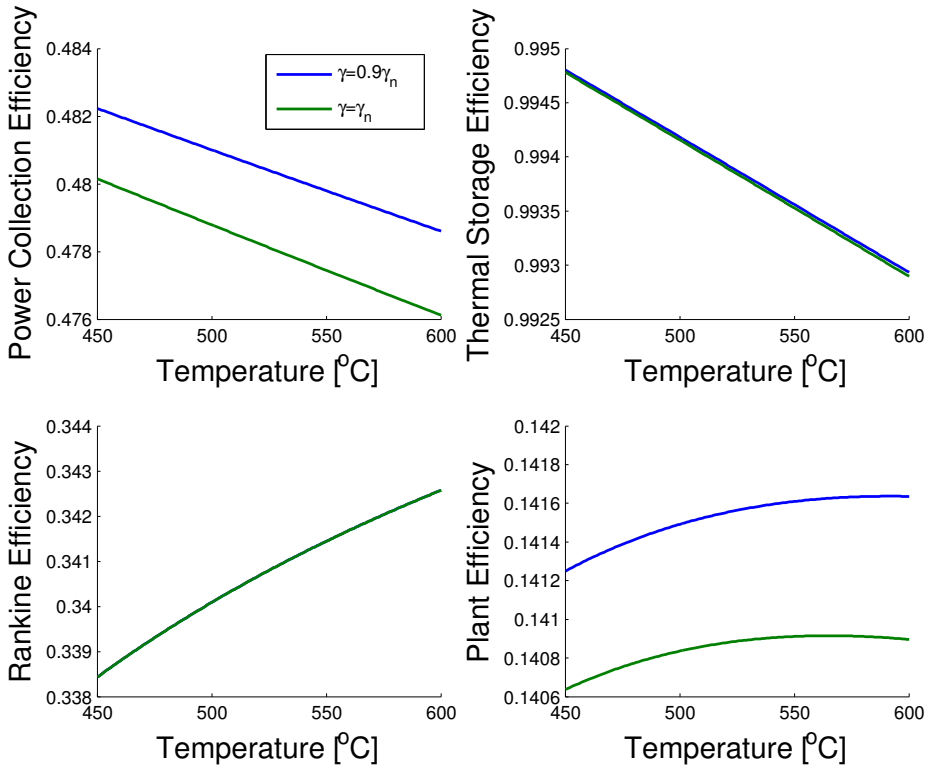

Figure 5.3: Power collection, thermal storage, Rankine cycle and overall plant efficiency for different receiver thermal loss coefficients.

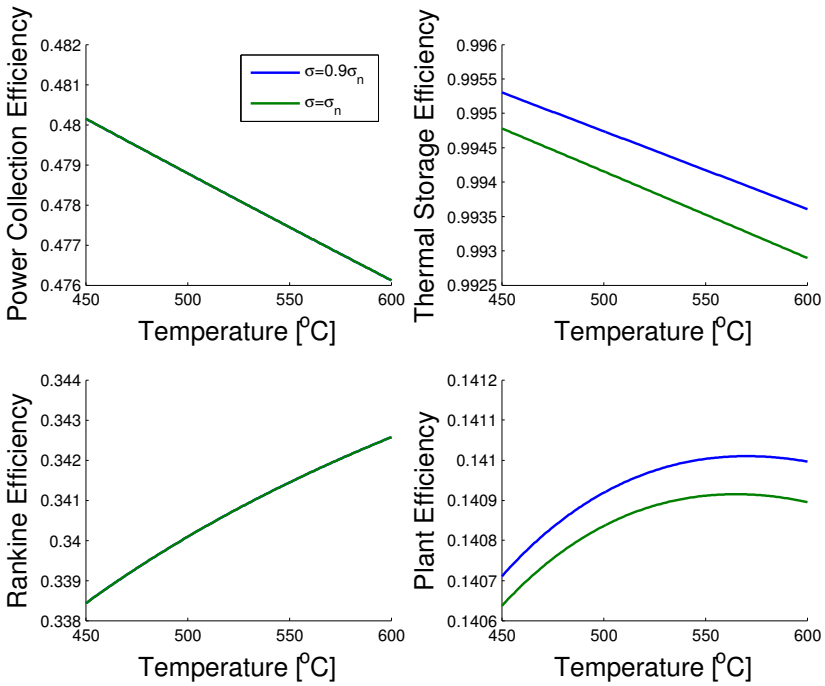

Figure 5.4: Power collection, thermal storage, Rankine cycle and overall plant efficiency for different thermal storage loss coefficients.

The effect of varying the Rankine cycle performance index is illustrated in figure 5.5. The increase of K rises the plant efficiency however, the optimal set-point is kept constant. In contrast, the reduction of the condenser temperature increases the Rankine and solar tower efficiencies, as shown in figure 5.6.

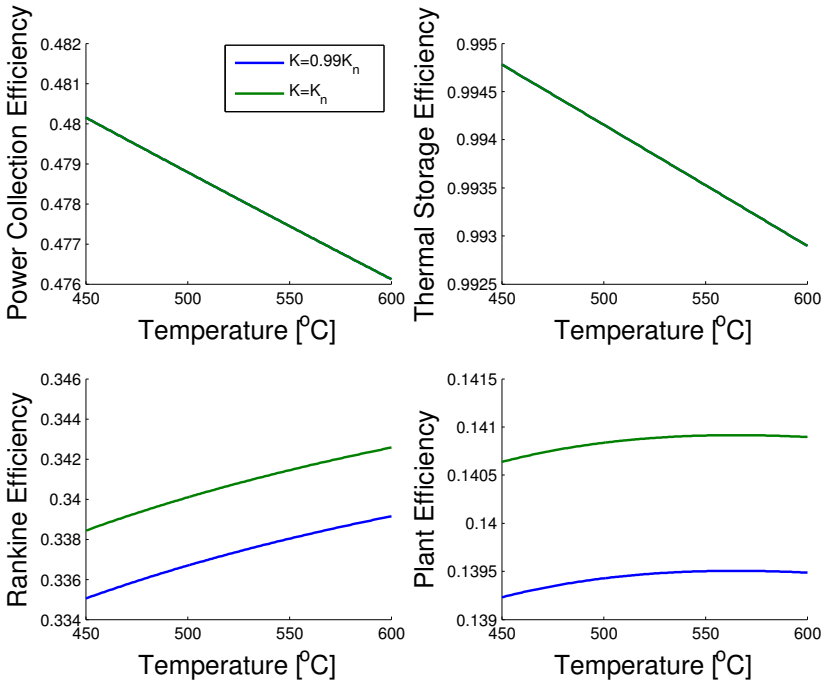

Figure 5.5: Power collection, thermal storage, Rankine cycle and overall plant efficiency for different Rankine Cycle Performance Index.

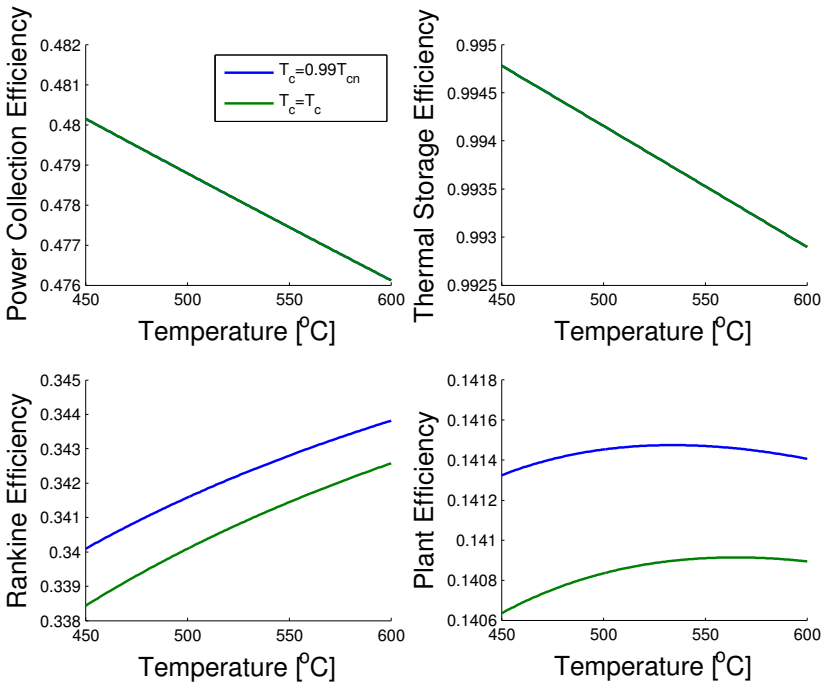

Figure 5.6: Power collection, thermal storage, Rankine cycle and overall plant efficiency for different condenser temperature.

The presented analysis indicates the need of a static-optimization supervisor that stipulates the outlet temperature set-point according to plant parameters and disturbances, since their change modifies the optimal operating temperature.

5.2.1 Elasticity

The electrical power production loss due to the nonlinear model parameters or coefficients estimation errors is evaluated through elasticity analysis. The latter is defined as a measurement of how an independent variable alters the dependent one, considering small changes relative to the nominal condition. The elasticity E of the electrical power produced P relative to a parameter or coefficients λ is given by [25],

$$E = \frac{\%\Delta P}{\%\Delta \lambda}. \tag{5.16}$$

The designed plant working condition has an overall peak efficiency for $T = 565^{o}C$ however, if a parameter is incorrectly estimated, the static optimization algorithm yields a set-point error that lowers the solar tower power production. Figure 5.7 illustrates the aforementioned proposition.

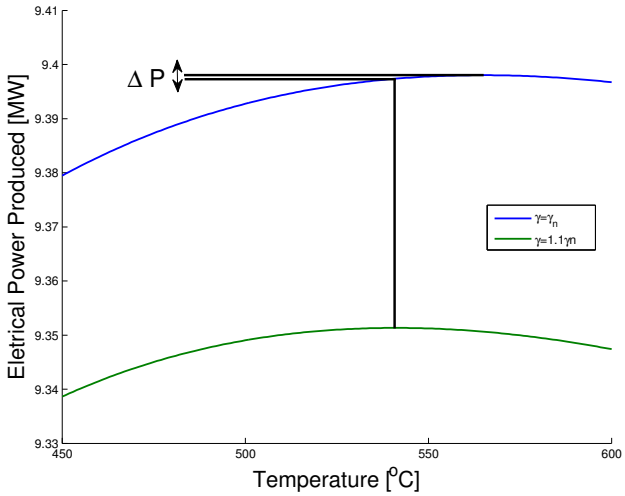

Figure 5.7: Power loss due to a parameter or coefficient estimation error.

Figures 5.8, 5.9,5.10 and 5.11 show the electrical power loss and respective elasticity regarding to the increase and decrease of the loss coefficient and absorption parameter. The dependent variable rises with any variation of γ or α however, the impact at the output is superior when their value decreases. Furthermore, the estimation error of α leads to higher losses.

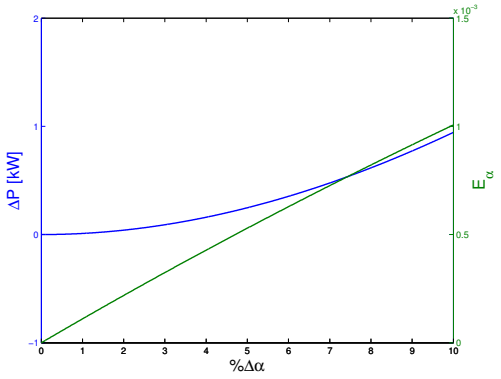

Figure 5.8: Electrical power loss and elasticity relative to the increase of α.

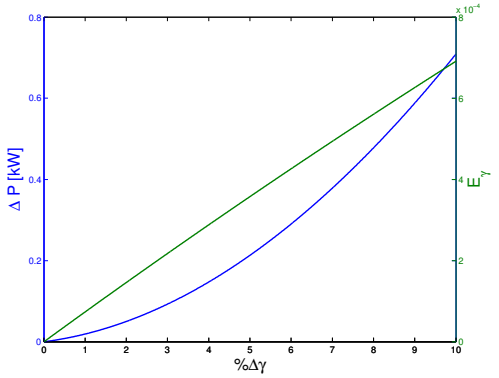

Figure 5.9: Electrical power loss and elasticity relative to the increase of γ.

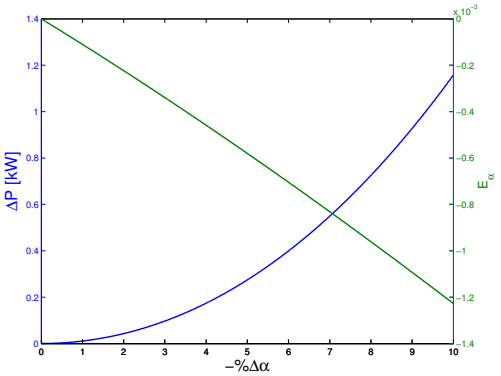

Figure 5.10: Electrical power loss and elasticity relative to the decrease of α.

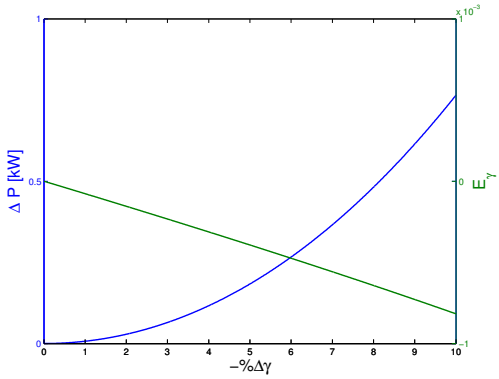

Figure 5.11: Electrical power loss and elasticity relative to the decrease of γ.

The measure error of the radiation flux also affects the plant output power. Figure 5.12 and 5.13 illustrate the the electrical power loss and elasticity relative to R. Similarly to γ and α, the decrease of the independent variable lowers the plant efficiency.

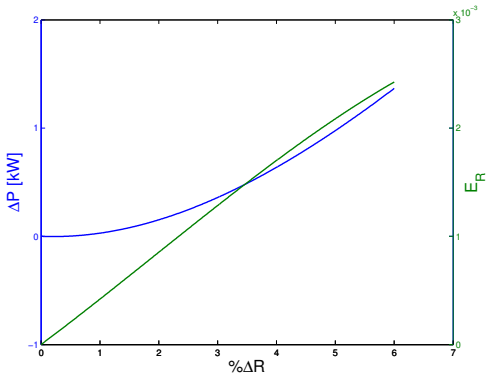

Figure 5.12: Electrical power loss and elasticity relative to the increase of R.

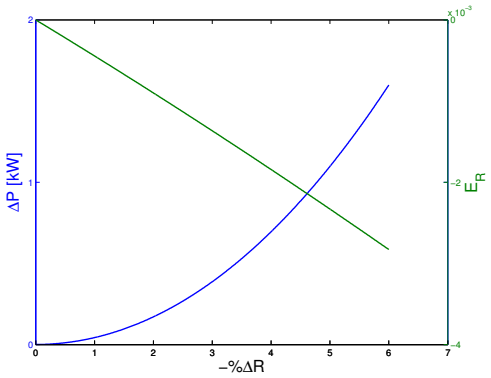

Figure 5.13: Electrical power loss and elasticity relative to the decrease of R.

The above elasticity study yields the conclusion that the reduced complexity model is robust to parameters estimation errors. The maximum power loss occurs for $\Delta\alpha = -10\%$ and only corresponds to approximately 0.0123% of the overall power produced, in the absence of estimation errors.

6

Simulation Results

Contents

The controllers performance when rejecting solar radiation disturbance in order to maintain the desired outlet temperature is now evaluated. The simulation experiments are performed for different sorts of reference and disturbance characteristics. The controlled system robustness to changing parameters or plant configuration is also examined. Furthermore, the on-line application of the static optimization algorithm is presented.

6.1 Solar Radiation Disturbance

The solar radiation disturbance varies in time due to the apparent movement of the sun, atmospheric moisture or passing clouds. The first two are conjointly assessed, whether the latter is examined separately. The controller tracking capability is evaluated considering equal solar radiation over the receiver surface. The temperature variance at the heat exchanger affects the plant lifetime thus, it is a weighting factor when selecting the proper controller. The requirement for a plant lifetime of 20-30 years is briefly verified.

6.1.1 Atmospheric Moisture

The solar tower receiver is constantly perturbed by atmospheric moisture that cause fast solar radiation variation of low amplitude linked with the apparent movement of the sun, as shown in figure 6.1.

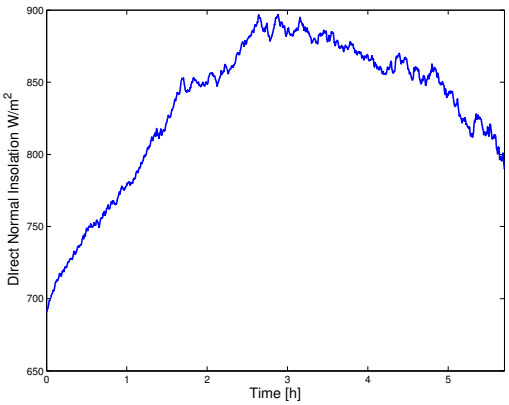

Figure 6.1: Solar radiation variation due to atmospheric moisture and the apparent movement of the sun.

The controllers performance at regulating the outlet temperature for $T = 565^oC$ in the absence of the feed-forward action, while the plant is disturbed with atmospheric moisture and the apparent movement of the sun is illustrated in figure 6.2. With the exception of the coordinated controlled system, the outlet temperature has an offset due to the sun's movement. Such perturbation is a ramp type disturbance that cannot be handled with only one integrator at the controller. However, the coodrinated controlled system that makes use of two manipulated variables is able to compensate the aforementioned offset. The latter system controlled variable has a lower variance although, it causes an increased wear of the heliostat field, since the flow is nearly constant. The LQG and the

MUSMAR controllers produce a similar response. From the controllers that only manipulate the flow, the PI controlled system is the most capable of rejecting solar radiation disturbances.

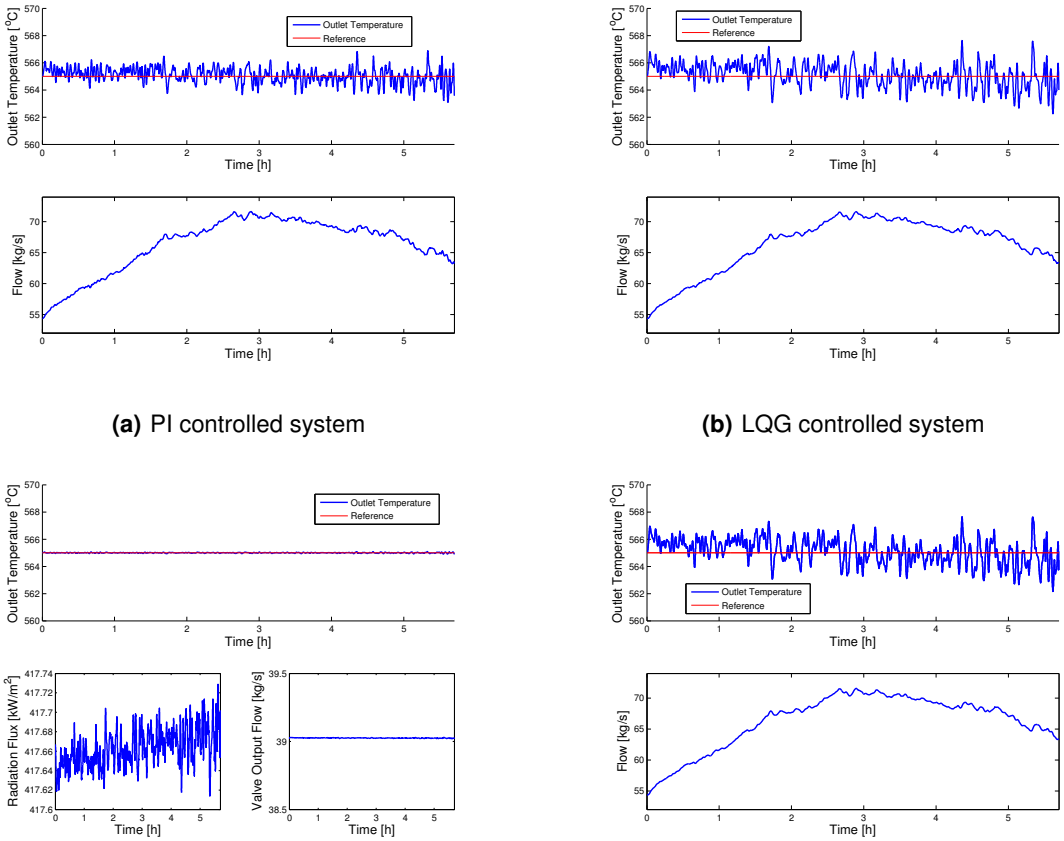

(a) PI controlled system

(b) LQG controlled system

(c) Coordinated controlled system

(d) MUSMAR controlled system

Figure 6.2: Controlled system set-point tracking in presence of the solar radiation variation due to atmospheric moisture and the apparent movement of the sun.

Performing the same regulation experiment while considering the feed-forward action is illustrated in figure 6.3. The outlet temperature variance is inferior than in the absence of feed-forward action. Also, the output offset is eliminated for the PI and LQG controllers. The MUSMAR controlled system has a constant deviation from the set-point below one degree and generates a superior excitation at the output and manipulated variables.

The coordinated controller does not makes use of the feed-forward signal therefore, it has not been included at the above analysis.

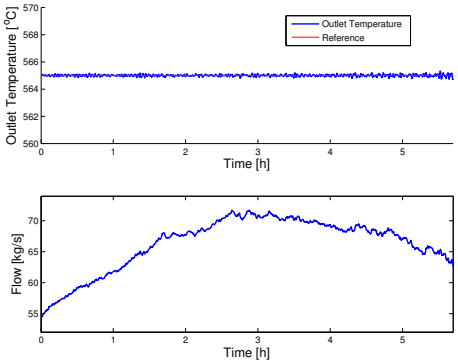

(a) PI controlled system

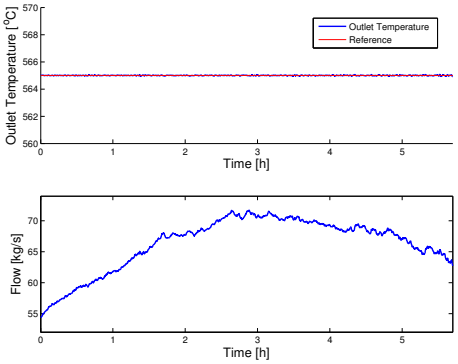

(b) LQG controlled system

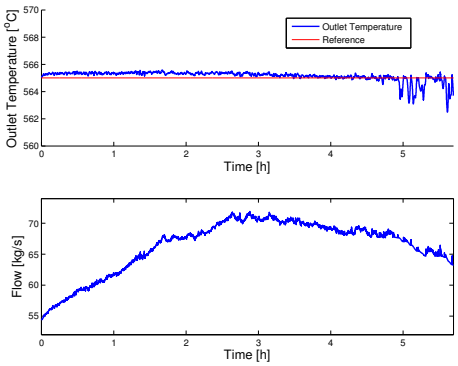

(c) MUSMAR controlled system

Figure 6.3: Controlled system with feed-forward action set-point tracking in presence of the solar radiation variation due to atmospheric moisture and the apparent movement of the sun.

The outlet temperature distribution over T for the regulation experiment is illustrated in figure 6.4. It can be concluded that the coordinated controlled system maintains the outlet temperature at the desired reference for longer time . The MUSMAR has the controlled variable more disperse although, it can be considered that the former is centred since the major variance occurs within half degree. The presented and remaining analysis is conducted considering the the feed-forward action for the PI, LQG and MUSMAR controllers.

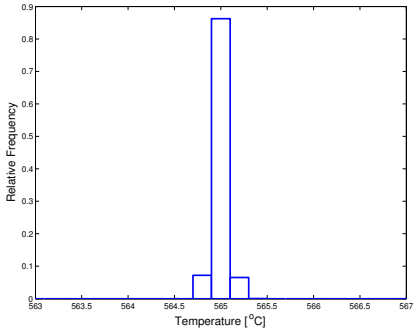

(a) PI controlled system

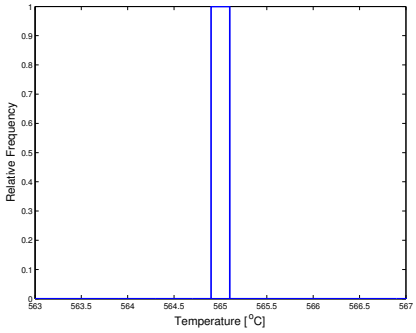

(b) LQG controlled system

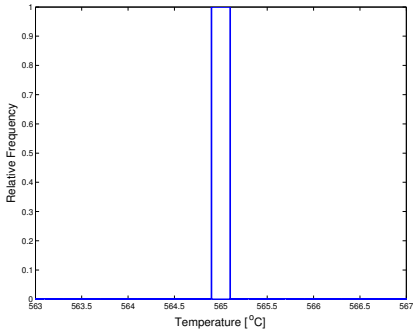

(c) Coordinated controlled system

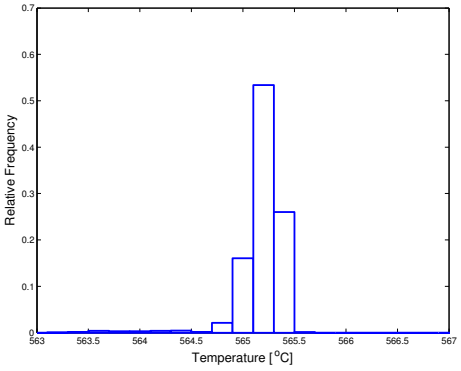

(d) MUSMAR controlled system

Figure 6.4: Outlet temperature distribution of the regulation experiment for $T = 565^oC$, in presence of the solar radiation variation due to atmospheric moisture and the apparent movement of the sun.

The controlled systems response to reference steps are illustrated in figure 6.5. The PI method changes between operating conditions more rapidly however, the optimal and coordinated controllers have an increased tracking capability at any working temperature. Although the output variable follows the reference with all controllers, the use of MUSMAR yield a superior rise time and variance. The latter and the coordinated control strategy leads to a lower wear of the actuator.

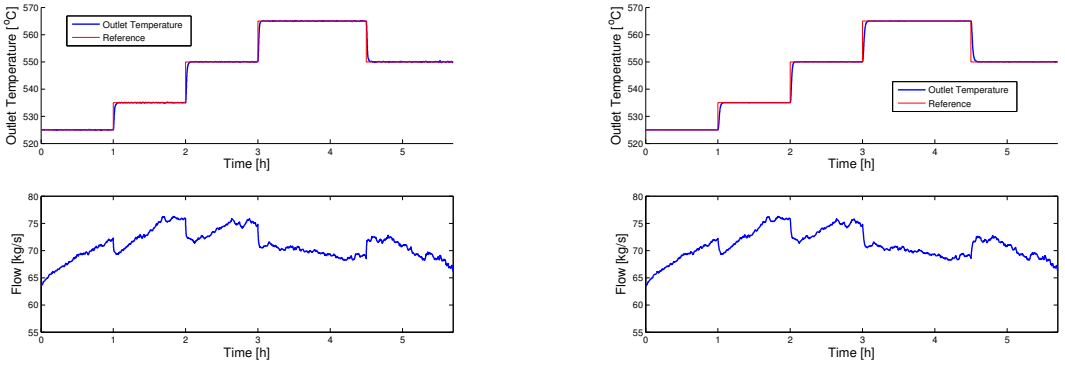

(a) PI controlled system

(b) LQG controlled system

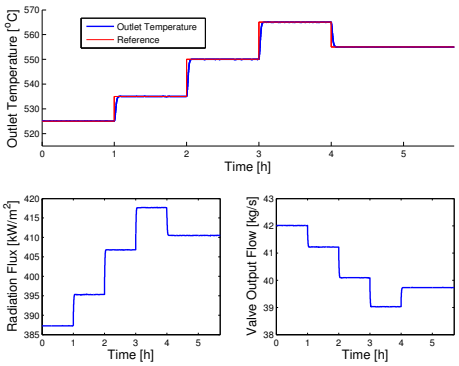

(c) Coordinated controlled system

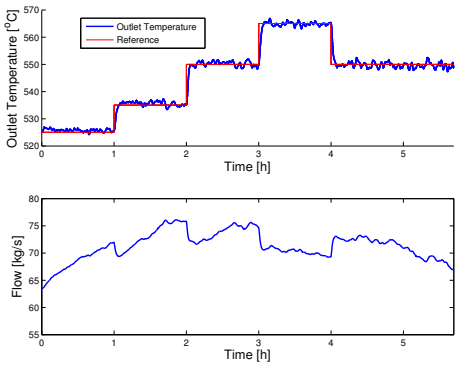

(d) MUSMAR controlled system

Figure 6.5: Controlled system step response through different operating conditions in presence of the solar radiation variation due to atmospheric moisture and the apparent movement of the sun.

6.1.2 Passing Clouds

The solar tower receiver can be perturbed by passing clouds that cause fast solar radiation variation of high amplitude and so, they are the most harmful to the infrastructure. Figure 6.6 illustrate the aforementioned disturbance.

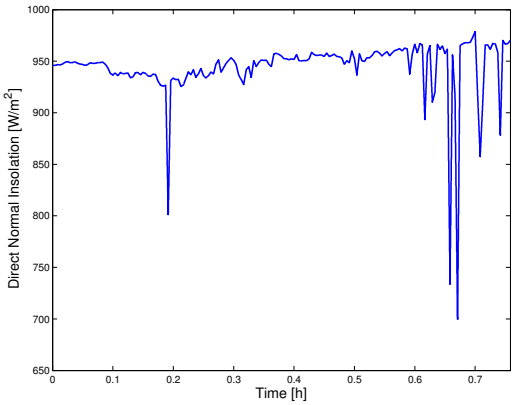

Figure 6.6: Solar radiation variation due to passing clouds.

The controllers capability to regulate the outlet temperature for $T = 565^oC$, while the plant is disturbed with passing clouds is illustrated in figure 6.7. The outlet temperature peak is more aggravating when using MUSMAR controller. On the other hand, the output variable maximum variance is lower for the coodrinated controlled system. The two last mentioned controllers yield a lower valve stress although, the latter generates an increased excitation at the heliostat field. The PI and optimal controllers are able to avoid large outlet temperature peaks when in presence of passing clouds however, the actuator lifetime is adversely affected. Table 6.1 identifies the maximum and minimum outlet temperature values obtained with each controlled system.

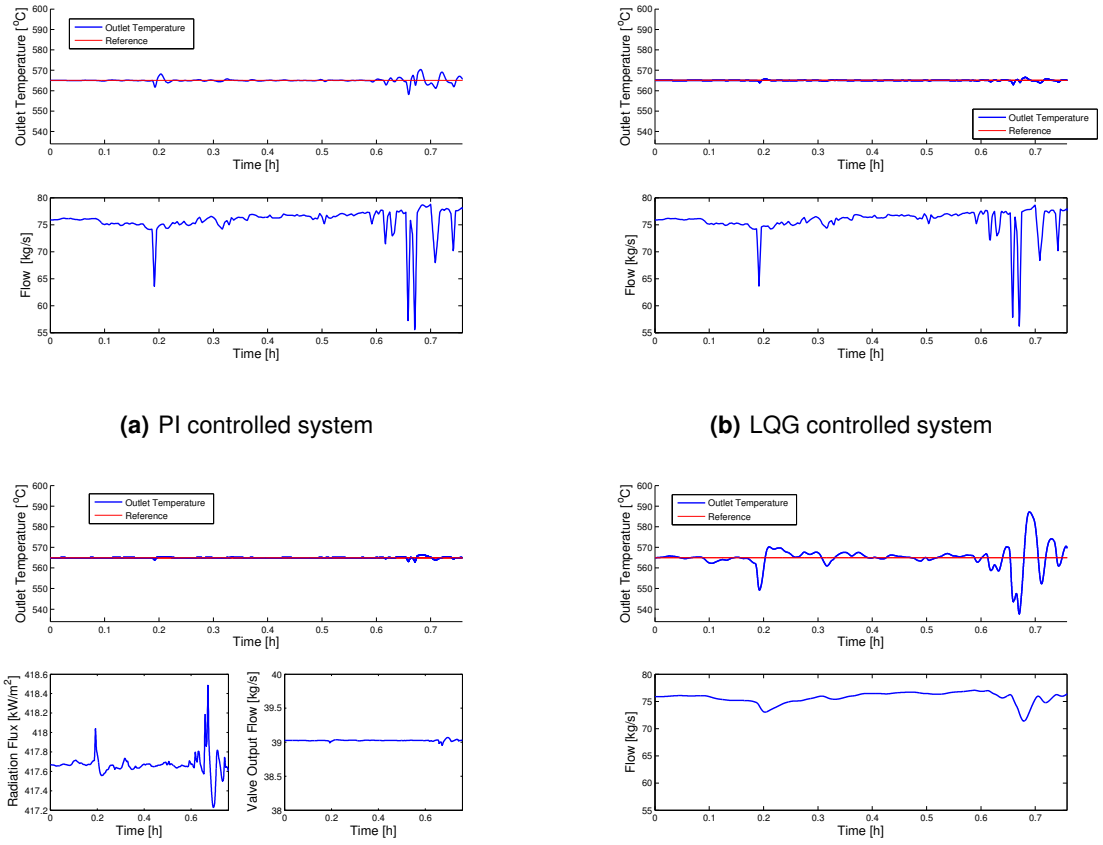

(a) PI controlled system

(b) LQG controlled system

(c) Coordinated controlled system

(d) MUSMAR controlled system

Figure 6.7: Controlled system response to set-point tracking for $T = 565^oC$ in presence of the solar radiation variation due to passing clouds.

Table 6.1: Outlet temperature limit values of the controlled system when disturbed by passing clouds.

	Outlet temperature limit values [^oC]							
	PI		**LQG**		**MUSMAR**		**Coordination**	
Disturbance	max	min	max	min	max	min	max	min
Passing Clouds	570.4	558.5	566.5	563.9	587.2	537.7	566.2	563.1

6.1.3 Lifetime

The lifetime of the receiver system is affected by the temperature rate of change at the tubes. In order to guarantee a lifetime of approximately 30 years, the latter rate must be less than 2.8$^oC/sec$ [22]. Table **??** details the outlet temperature rate of change when the system is perturbed with atmospheric moisture and passing clouds. The determined values yield the conclusion that the controllers meet the expectations by a large margin. The lowest temperature rate of change is achieved when using the coordinated controller.

The significance of the obtained data is dependent on the pump considered and the use of high quality sensors. Moreover, since the flux distribution at the receiver is not homogeneous , a different temperature rate of change can be found at the middle of the heat exchanger tubes.

Table 6.2: Outlet temperature rate.

	Outlet temperature rate [^oC/s]							
	PI		**LQG**		**MUSMAR**		**Cordination**	
Disturbance	max	mean	max	mean	max	mean	max	mean
Atmospheric Moisture	0.007	0.003	0.022	7.560×10^{-4}	0.05 0	0.005	0.005	7.260×10^{-4}
Passing Clouds	0.630	0.039	0.634	0.017	1.692	0.108	1.650	0.095

6.2 Controller Robustness

The controller robustness is assessed by analysing the change of controlled system performance when a parameter or coefficient is modified. Also, it is examined the controller ability to handle a valve fault.

6.2.1 Parameter

The controller robustness to parameter change is evaluated by varying the absorption and mirror efficiency α and the loss coefficient γ of the reduced complexity model. The comparison between the outlet temperature distribution of the nominal and modified parameter provides information regarding to the controller performance change. Figure 6.8 illustrate the a controlled variable distribution obtained by decreasing α in 20%, when the plant is perturbed with solar radiation variation due to atmospheric moisture and the apparent movement of the sun. The increase of the latter parameter cause a minor effect at the system. The controlled processes have a temperature distribution more dispersed than the nominal case, shown in figure 6.4. The exception occurs when using the coordinated control strategy that maintains a centred temperature allocation. Such behaviour is verified since the manipulation of the radiation flux is able to compensate the reduction of α. The MUSMAR controlled variable becomes more centred due to the controller gains adaptation. However, for a higher parameter change, the temperature distribution becomes flatter between the boundary values of $T = 564.5^oC$ and $T = 565.5^oC$.

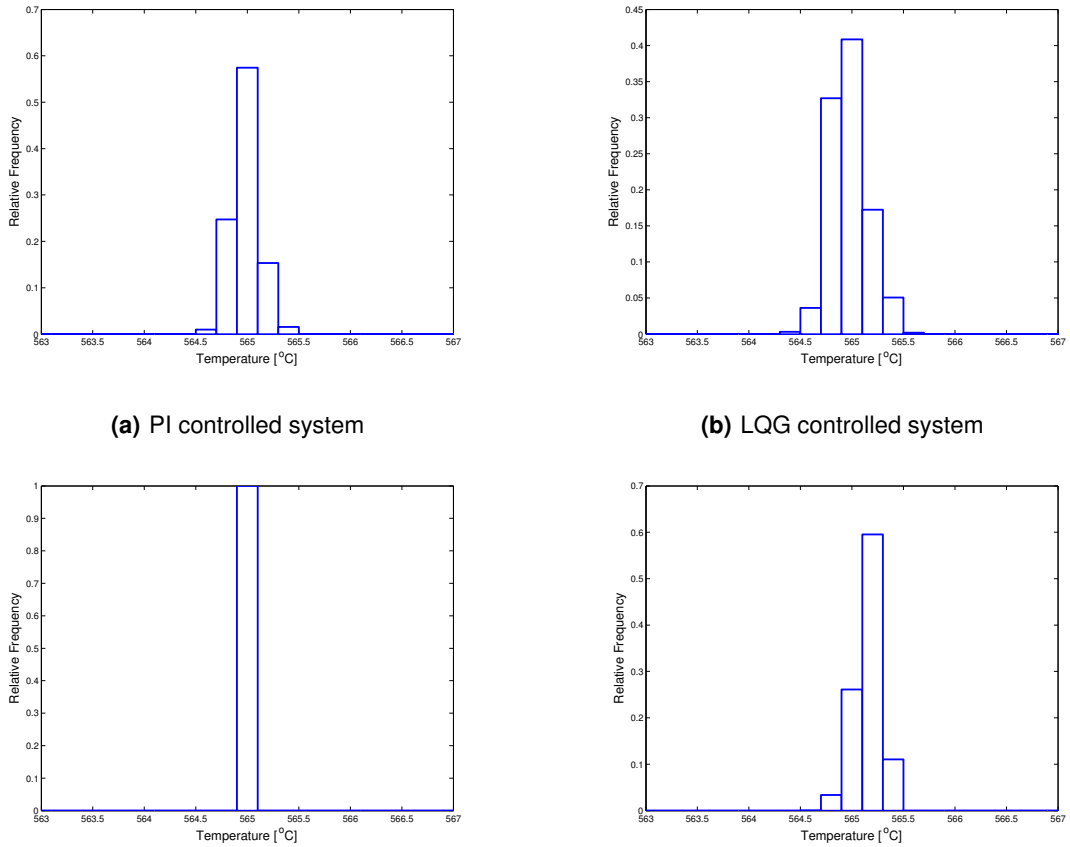

(a) PI controlled system

(b) LQG controlled system

(c) Coordinated controlled system

(d) MUSMAR controlled system

Figure 6.8: Outlet temperature distribution of the regulation experiment for $T = 565^oC$, in presence of the solar radiation variation due to atmospheric moisture and the apparent movement of the sun, when α decreases 20%.

Figure 6.9 illustrate the outlet temperature variance obtained by increasing γ in 20%. The PI, LQG and the coordinated controlled systems do not exhibit significant changes when comparing to the use of the nominal value of γ. The MUSMAR controlled variable becomes more flat yet not dispersed.

It can be concluded that the coefficient in analysis has a minor impact at the controlled variable than α.

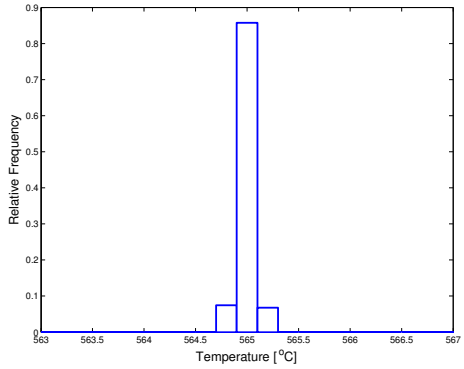

(a) PI controlled system

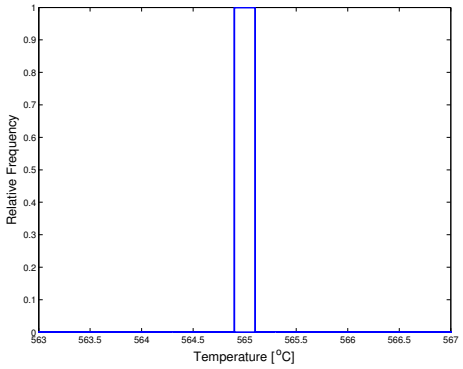

(b) LQG controlled system

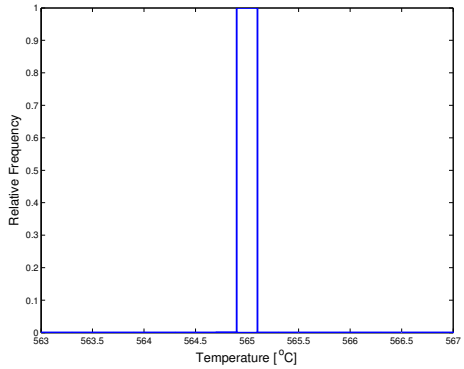

(c) Coordinated controlled system

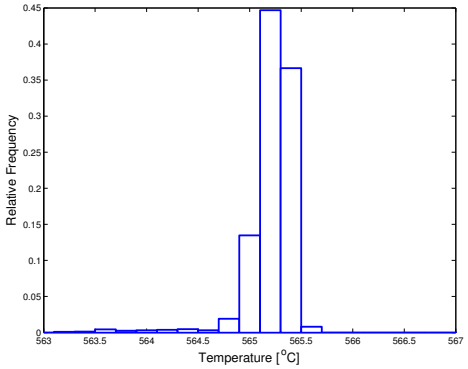

(d) MUSMAR controlled system

Figure 6.9: Outlet temperature dispersion of the set-point tracking experiment for different controlled systems when γ increases 20%, in presence of the solar radiation variation due to atmospheric moisture and the apparent movement of the sun.

Although the controller performance is affected by parameters change, the variance of the outlet temperature is only two degrees at maximum when the solar radiation disturbance is due to atmospheric moisture. It is to remember that the model is also robust.

6.2.2 Valve Fault

The controller robustness to a valve fault is conducted by analysing the situation when the flow stops abruptly at a given receiver circuit path. After the actuator failure, it is considered that the heliostat field takes approximately 4 s to defocus from the heat exchanger area where the circuit is installed. Figure 6.10 illustrates the controlled system response to the aforementioned fault. The coordinated controlled system has a smoother outlet temperature response to the valve fault however, the output variance is high. The MUSMAR controlled variable has an even superior temperature peak although, the transition is soft and the time required to recover to the desired set-point is the lowest. The use of PI and LQG controllers lead to an oscillatory outlet temperature response that reduces the receiver lifetime. Also, it can be seen that variance of the controlled variables of the aforementioned systems increase after the fault recovery. The MUSMAR controller is able to maintain the performance prior to the failure.

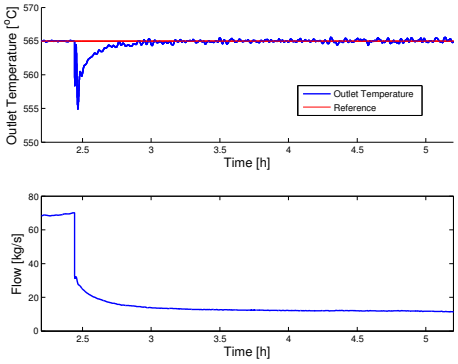

(a) PI controlled system

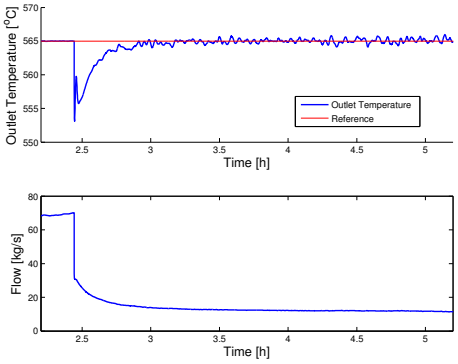

(b) LQG controlled system

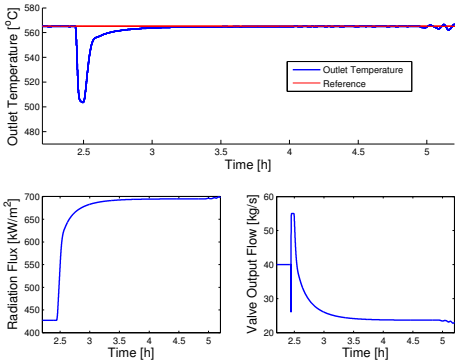

(c) Coordinated controlled system

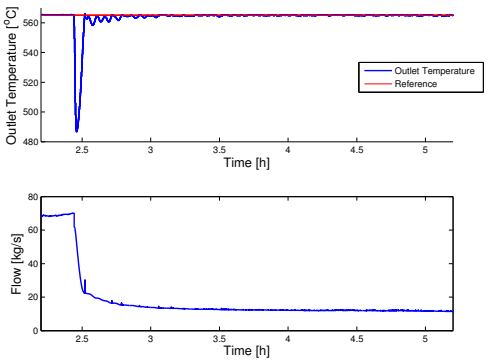

(d) MUSMAR controlled system

Figure 6.10: Controlled system response to a fault at one circuit flow while tracking a constant reference, in presence of the solar radiation variation due to atmospheric moisture and the apparent movement of the sun.

6.3 On-line Static Optimization

The static optimization algorithm developed in chapter 5 is now applied to the reduced complexity model while considering the PI controller as the second layer of the optimal operation control structure. The optimal outlet temperature reference is stipulated every 10 minutes. Figure 6.11 illustrate the solar radiation disturbance used.

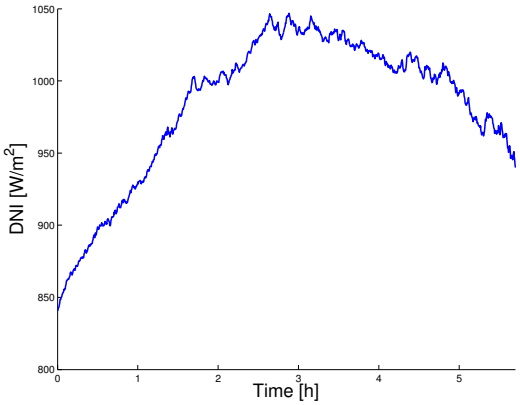

Figure 6.11: Solar radiation variation used to analyse the optimal operation control system.

The outlet temperature reference given by the static optimization algorithm and the PI controlled variable in conjunction with the flow are shown in figure 6.12. As expected, the increase of DNI leads to a rise of the optimal output reference while the opposite is verified when the solar radiation decreases. Figure 6.13 illustrate the controlled and manipulated variable obtained when the reference is $T = 565^oC$. It can be seen that the flow varies between a wider range of values however, the valve output time evolution is more smooth.

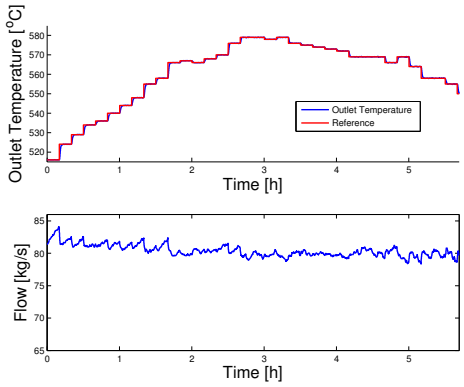

Figure 6.12: Controlled and manipulated variables when the outlet temperature reference is given by the static optimization algorithm.

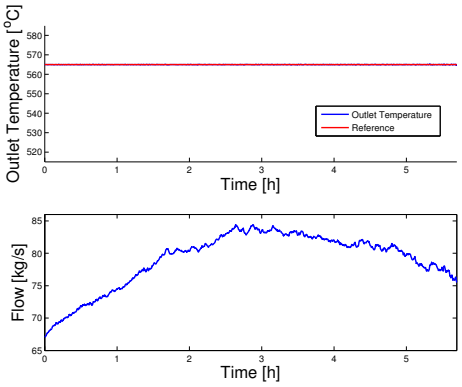

Figure 6.13: Controlled and manipulated variables obtained when the outlet temperature reference is set to $T = 565^oC$.

Figures 6.14 and 6.15 illustrate the electrical energy produced when using the last mentioned references. The results are similar although, the use of the nominal reference yields an increased electrical energy production of 6 kWh, at the end of the day. Figures 6.16 and 6.17 illustrate the plant output power. In order to track the optimal reference, the flow needs to decrease. However, since the manipulated variable diminishes faster than the outlet temperature rises, a loss of electrical production is verified. The opposite is verified when the reference decreases. Therefore it can be concluded that the fluid dynamics must be considered when optimizing the plant power production.

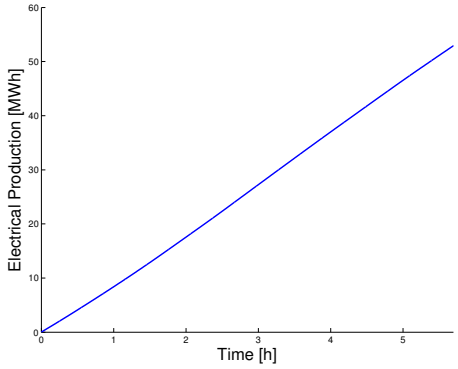

Figure 6.14: Electrical energy produced obtained when the outlet temperature reference is given by the static optimization algorithm.

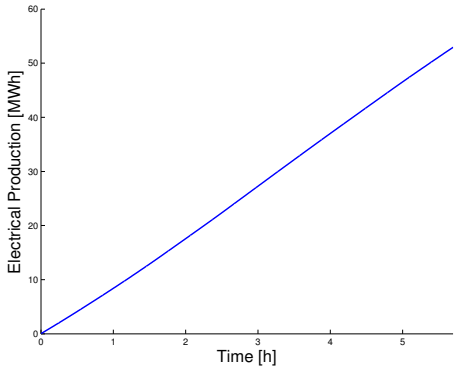

Figure 6.15: Electrical energy produced when the outlet temperature reference is set to $T = 565^oC$.

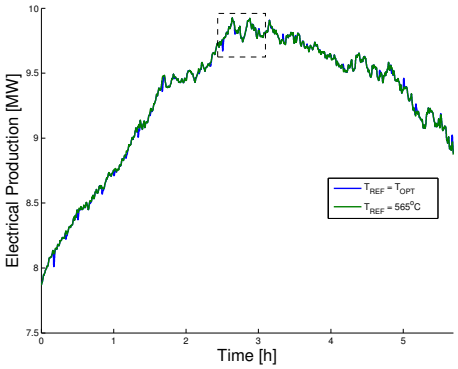

Figure 6.16: Electric power generated when the outlet temperature reference is given by the static optimization algorithm and $T = 565^oC$.

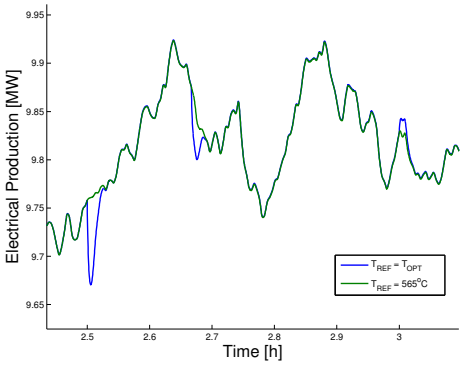

Figure 6.17: Electric power generated when the outlet temperature reference is given by the static optimization algorithm and $T = 565^oC$.

7

Conclusions

Contents

7.1 Main Points

The presented master thesis focus on the fluid outlet temperature model and control of a solar tower heat exchanger. The first purpose is achieved by projecting the spacial dependence of a infinite nonlinear partial differential equation model based on physical principles, on a finite dimensional set. The second aim is accomplished by developing a PI, LQG, MUSMAR and a coordinated controller. Moreover, it is established a static optimization algorithm that determines the outlet temperature set-point that leads to the maximum plant power production.

The PI linear controller is developed for several working conditions of the plant nonlinear reduced complexity model wherein the controller parameters are design using a modified Ziegler and Nichols ultimate sensitivity rule. The latter tuning method uses the ultimate gain and period that are determined through the relay with hysteresis feedback procedure. The LQG controller is based on a discrete linear model obtained through system identification using data collected from the nonlinear model, while functioning near the operating regime.

The process nonlinear dynamics is handled by using a GS scheme for the PI controller, where its gains are given as a function of the outlet temperature. For the LQG, it is developed a multi-model adaptive control strategy in which one of a set of LQG controllers is selected to generate the control signal. The transition between the former systems is accomplished by initializing the integrator of the controller to be connected, avoiding transition bumps. In addition, the solar radiation disturbance rejection capability is increased by designing a static feed-forward controller to work in parallel with the aforementioned control systems.

The MUSMAR controller is implemented after configuring its parameters by minimizing a quadratic cost function and observing the controlled and manipulated variables characteristics. The coordinated control strategy that uses the flow and the radiation flux as manipulated variables is designed using the PI control concept with manually adjusted gains. Also, a GS scheme is developed for the former approach.

Subsequent to the controllers development, it is examined their performance by analysing the experimental results obtained through simulation by applying different sorts of reference and solar radiation disturbance characteristics. The regulation of the outlet temperature in presence of the solar radiation variation due to atmospheric moisture and the apparent movement of the sun yields a centred outlet temperature distribution for all controllers, when using the feed-forward action. The improved and worsened results of the aforementioned experiment are achieved while using the optimal or coordinated controller and the MUSMAR algorithm, respectively.

The controlled systems step response provide best results for the optimal control in what concerts the output variable tracking capability however, the use of coordinated control leads to a minor wear of the actuator. Moreover, the latter controller has an outlet temperature fluctuation similar to the LQG.

The regulation of the outlet temperature in presence of the solar radiation variation due to passing clouds are best handled by coordinated control. The PI and LQG also have a low temperature variance however, the actuator is strongly exited. The MUSMAR controlled variable varies between a

larger temperature scale, the valve is less fatigued.

The analyses of the controller robustness to changing parameters while considering the regulation problem yields the conclusion that the outlet temperature distribution becomes more disperse, although it only increases half degree for a change in 20% of the heat exchanger absorption and mirror efficiency parameter, that is the most sensible. The coordinated control it is not affected by such change since the radiation flux is manipulated. The MUSMAR controlled variable becomes less disperse however, more flatter.

The controllers robustness to a fault in one valve demonstrates that the MUSMAR and the coordinated controlled systems have a high temperature drop although, the actuator has a smooth behaviour. The MUSMAR controller recovers to the nominal operating condition faster and is able to maintain the performance prior to the failure. In contrast, the PI and LQG controlled variables have an oscillatory behaviour.

The analysis of the outlet temperature rate of change yields the conclusion that the lifetime of 20-30 years is guaranteed, although, the data significance is dependent on the pump considered and the use of high quality sensors.

The application of the static optimization algorithm yielded poor results in several cases since the fluid dynamics is not considered in such approach.

7.2 Future Work

The dimension of the finite spatial dimensional set where the reduced complexity model was projected must be examined to determine the number of points that yields a more accurate model.

The coordinated control strategy developed provided good results however, it must be studied with different control strategies while considering a closer representative model of the heliostat field.

The temperature set-point optimization can achieve better results if the dynamic behaviour of the plant is considered. Also, the consideration of the wind influence in in thermal losses may lead to different conclusions from applying the static optimization algorithm.

Bibliography

[1] R. W. Bradshaw, D. B. Dawson, W. De la Rosa, R. Gilbert, S. H. Goods, M. J. Hale, P. Jacobs, S. a. Jones, G. J. Kolb, J. E. Pacheco, M. R. Prairie, H. E. Reilly, S. K. Showalter, and L. L. Vant-Hull, "Final Test and Evaluation Results from the Solar Two Project," *Contract*, no. January, p. 294, 2002.

[2] H. E. Reilly and G. J. Kolb, "An evaluation of molten-salt power towers including results of the solar two project," *Sandia National Laboratories*, pp. 1–94, 2001.

[3] J. M. Lemos, João M., Neves-Silva, Rui, Igreja, *Adaptive Control of Solar Energy Collector Systems*. Springer, 2014.

[4] K. J. Astrom and B. Wittenmark, *Computer Controlled Systems*, 1997.

[5] W. a. Hermann, "Quantifying global exergy resources," pp. 1349–1366, 2006.

[6] M. J. Wagner, "Simulation and Predictive Performance Modeling of Utility-Scale Central Receiver System Power Plants by," p. 259, 2008. [Online]. Available: http://sel.me.wisc.edu/publications/theses/wagner08.zip

[7] U.S Department of Energy, "Concentrating Solar Power - Point Focus Reflector Technologies," 2008. [Online]. Available: http://solareis.anl.gov/documents/docs/NREL_CSP_2.pdf

[8] E. F. Camacho, F. R. Rubio, M. Berenguel, and L. Valenzuela, "A survey on control schemes for distributed solar collector fields. Part I: Modeling and basic control approaches," *Solar Energy*, vol. 81, no. 10, pp. 1240–1251, 2007.

[9] D. Sworder and R. Rogers, "An LQ-solution to a control problem associated with a solar thermal central receiver," *IEEE Transactions on Automatic Control*, vol. 28, no. 10, pp. 971–978, 1983.

[10] C. M. Cirre, L. Valenzuela, M. Berenguel, and E. F. Camacho, "Feedback linearization control for a distributed solar collector field," *IFAC Proceedings Volumes (IFAC-PapersOnline)*, vol. 16, pp. 356–361, 2005.

[11] M. Barão, J. M. Lemos, and R. N. Silva, "Reduced complexity adaptive nonlinear control of a distributed collector solar Â® eld," *Journal of Process Control*, vol. 12, pp. 131—-141, 2002.

[12] A. Orbach, C. Rorres, and R. Fischl, "Optimal control of a solar collector loop using a distributed-lumped model," 1981. [Online]. Available: http://www.sciencedirect.com/science/article/pii/0005109881900108

[13] R. N. Silva, J. M. Lemos, and L. M. Rato, “Variable sampling adaptive control of a distributed collector solar field,” *Control Systems Technology, IEEE Transactions on*, vol. 11, no. 5, pp. 765–772, 2003.

[14] a. Meaburn and F. Hughes, “Resonance characteristics of distributed solar collector fields,” *Solar Energy*, vol. 51, no. 3, pp. 215–221, 1993.

[15] M. Berenguel and E. Camacho, “Frequency-based adaptive control of systems with antiresonance modes,” *Control Engineering Practice*, vol. 4, no. 5, pp. 677–684, 1996. [Online]. Available: http://www.sciencedirect.com/science/article/pii/0967066196000512

[16] M. Berenguel, M. R. Arahal, and E. F. Camacho, “Modelling the free response of a solar plant for predictive control,” *Control Engineering Practice*, vol. 6, no. 10, pp. 1257–1266, 1998.

[17] M. Pérez de la Parte, C. M. Cirre, E. F. Camacho, and M. Berenguel, “Application of predictive sliding mode controllers to a solar plant,” *IEEE Transactions on Control Systems Technology*, vol. 16, no. 4, pp. 819–825, 2008.

[18] a. Flores, D. Saez, J. Araya, M. Berenguel, and a. Cipriano, “Fuzzy predictive control of a solar power plant,” *IEEE Transactions on Fuzzy Systems*, vol. 13, no. 1, pp. 58–68, 2005.

[19] C. M. Cirre, M. Berenguel, L. Valenzuela, and R. Klempous, “Reference governor optimization and control of a distributed solar collector field,” *European Journal of Operational Research*, vol. 193, no. 3, pp. 709–717, 2009.

[20] E. F. Camacho and a. J. Gallego, “Optimal operation in solar trough plants: A case study,” *Solar Energy*, vol. 95, pp. 106–117, 2013.

[21] J. E. Pacheco, H. E. Reilly, G. J. Kolb, and C. E. Tyner, “Summary of the Solar Two test and evaluation program,” *Proceding of the Renewable Energy for the New Millenium*, pp. 1–11, 2000.

[22] A. B. Zavoico, “Solar Power Tower - Design Basis Document,” no. July, p. 148, 2001. [Online]. Available: http://prod.sandia.gov/techlib/access-control.cgi/2001/012100.pdf

[23] R. M. Murray, “Feedback Systems: An Introduction for Scientists and Engineers,” *The Quarterly Review of Biology*, vol. 83, no. 4, pp. 426–426, 2008. [Online]. Available: http://www.journals.uchicago.edu/doi/abs/10.1086/596297

[24] T. Astrom, K. & Hagglund, “PID Controllers: Theory, Design, and Tuning.” 1995.

[25] D. M. Hamby, “A review of techniques for parameter sensitivity analysis of environmental models.” *Environ. Monit. Assess.*, vol. 32, no. 2, pp. 135–154, 1994. [Online]. Available: http://deepblue.lib.umich.edu/handle/2027.42/42691

Discrete time ARMAX Linear Model

The discrete-time ARMAX linear model of the receiver fluid outlet temperature dynamics near the nominal operating condition, $F = 80kg/s$ and $T = 565^oC$, is given by,

$$A(q)y(k) = B(q)u(k) + C(q)e(k)$$

where,

$$A(q) = 1 - 2.851q^{-1} + 3.204q^{-2} - 1.68q^{-}3 + 0.3342q^{-}4 + 0.005195q^{-}5$$
$$+0.009046q^{-6} - 0.001996q^{-7} - 0.0003094q^{-8} - 0.003988q^{-9} + 0.001707q^{-10},$$

$$B(q) = -6724q^{-1} + 4264q^{-2} + 2358q^{-3} - 3721q^{-4},$$

$$C(q) = 1 + 0.3272q^{-1} - 0.02865q^{-2} + 0.5338q^{-3} + 0.4761q^{-4} + 0.3466q^{-5}$$
$$+0.1561q^{-6} + 0.008087q^{-7} - 0.06184q^{-}8 - 0.03408q^{-}9 - 0.007183q^{-10}.$$

B

Reduced complexity Model

The partial differential equation that describes the fluid temperature dynamics over one of the n_t tubes at receiver the circuit path is given by,

$$\frac{\partial}{\partial t}T(z,t) = -\frac{\dot{m}}{A_f}\frac{\partial}{\partial z}T(z,t) + \frac{\bar{\alpha}}{\rho c_f A_f}R(t) - \gamma(T_{av}(z,t) - Ta). \tag{B.1}$$

in which the variables description and nominal values are detail in table B.1.

The *MATLAB Simulink* model developed is based on a set of a series of ordinary differential equations for each path for $i = 1...n_P$,

$$\frac{dx_i}{dt} = -F(t)\frac{1}{\Delta z}(x_i(t) - x_{i-1}(t)) + \alpha R(t) - \gamma\Big(\frac{(x_i(t) + x_{i-1}(t)}{2} - T_a\Big). \tag{B.2}$$

where n_P is the number of panels, F is the fluid velocity of one tube,

$$F = \frac{\dot{m}}{A_f},$$

and α is defined as,

$$\alpha \triangleq \frac{\bar{\alpha}}{\rho_f c_f A_f}.$$

Thus, the output of the representative model is given by the following expression,

$$y(t) = \frac{F_P^1}{F_P^1 + F_P^2}x_n^1 + \frac{F_P^2}{F_P^1 + F_P^2}x_n^2, \tag{B.3}$$

where $x_n^{1,2}$ and $F_P^{1,2}$ is the outlet temperature and fluid velocity of each path, respectively. The flow of one receiver circuit corresponds to the flow F, multiplied by the number of tubes per panel.

Table B.1: Parameters and coefficients used to model the Solar Two receiver system.

Description	Symbol	Value
Inlet temperature	$T(0,t)$	290^oC
Outlet temperature	$T(L,t)$	565^oC
Absorption and mirror efficiency	$\bar{\alpha}$	$6.70 \times 10^{-3}\ m$
Loss coefficient	γ	$8.56 \times 10^{-4}\ s^{-1}$
Pipe cross-section area	A_f	$2.7172 \times 10^{-4}\ m$
Pipe element length	Δz	7.96 m
Flow circuit length	Δz	95.52 m
Number of panels	n_P	12
Number of tuber per panel	n_t	32
Nominal flow Rate	$\dot{m}_{nom}$	$6.5598 \times 10^{-4} m^3/s$
Maximum flow Rate	$\dot{m}_{max}$	$9.0197 \times 10^{-4} m^3/s$
Nominal incident radiation Flux	R	430 kW/m^2

The molten salt density ρ_f and specific heat c_f are given by,

$$\rho_f(T) = 2090 - 0.636 \times T, \qquad [\text{kg m}^{-3}] \tag{B.4}$$

$$c_f(T) = 1143 + 0.172 \times T, \qquad [\text{J kg}^{-1}\ ^\circ\text{C}^{-1}] \tag{B.5}$$